Editors' Suggestion

Interaction-induced charge transfer in a mesoscopic electron spectrometer

Stefan G. Fischer,[1,2] Jinhong Park,[2] Yigal Meir,[1] and Yuval Gefen[2]
[1]*Department of Physics, Ben-Gurion University of the Negev, Beer-Sheva, 84105 Israel*
[2]*Department of Condensed Matter Physics, Weizmann Institute of Science, Rehovot, 76100 Israel*

(Received 15 August 2019; published 8 November 2019)

In this paper, we theoretically investigate a mesoscopic electron spectrometer that allows for the probing of relaxation processes in quantum Hall edge channels, which has recently been experimentally realized. The device is composed of an emitter quantum dot that injects energy-resolved electrons into the channel closest to the sample edge, to be subsequently probed downstream by a detector quantum dot of the same type. In addition to inelastic processes in the sample that stem from interactions inside the region between the quantum dot energy filters (inner region), anomalous signals are measured when the detector energy exceeds the emitter energy. Considering finite-range Coulomb interactions in the sample, we find that energy exchange between electrons in the current-inducing source channel and the inner region, similar to Auger recombination processes, is responsible for such anomalous currents. In addition, our perturbative treatment of interactions shows that electrons emitted from the source, which dissipate energy to the inner region before entering the detector, contribute to the current most strongly when emitter-detector energies are comparable. Charge transfer in which the emitted electron is exchanged for a charge carrier from the Fermi sea, on the other hand, preferentially occurs close to the Fermi level.

DOI: 10.1103/PhysRevB.100.195411

I. INTRODUCTION

Coherent transport in chiral quantum Hall edge channels of mesoscopic devices is of considerable conceptual importance. Chiral channels enable the electronic implementation of originally optical interferometers, such as of the Fabry-Perot [1] or of the Mach-Zehnder [2,3] type. In the electronic versions of such devices, interference occurs between the paths of the respective quasiparticles, which may enable the observation of anyonic statistics in the fractional quantum Hall regime [4,5]. Moreover, the implementation of quantum computational operations using edge channels is conceivable [6].

Relaxation dynamics of the electronic system plays a crucial role for transport properties of quantum Hall edges. Generically, relaxation processes exert a detrimental influence on coherence properties of edge channels, such as, e.g., on the interferometers' fringe visibility [2,3,7–9]. In addition to the fundamental interest in the phenomenon, it is therefore desirable to acquire a comprehensive picture of possible mechanisms which contribute to relaxation of nonequilibrium charge carrier distributions.

To study relaxation properties of quantum Hall edge channels, le Sueur *et al.* [10] devised an experiment in which a quantum point contact induces a nonequilibrium distribution into the outermost of two edge channels, which is energetically probed downstream by a quantum dot. During propagation, interactions between the outer and inner channels cause relaxation of the initial distribution. Surprisingly, a significant amount of energy induced into the setup is lost to inaccessible degrees of freedom [11–13]. A further experiment [14] to study relaxation in edge channels, that controls the energy of quasiparticle excitations by a microwave-frequency circuit, probes intermediate relaxation by means of a downstream Ohmic contact. The modes of the channels are found to be dissipative, while also in this setup the degrees of freedom that absorb the dissipated energy remain undetermined.

At the ETH Zürich an electron spectrometer was used to probe energetic relaxation in edge channels by means of two successive quantum dots in a novel experiment to identify relaxation mechanisms in quantum Hall edges [15,16]. A similar setup has also been realized with shorter propagation paths [17]. A typical sample, as depicted in Fig. 1(a), is composed of a source and a drain lead, coupled to an intermediate reservoir via an emitter and a detector quantum dot. The quantum dots act as energy filters for incoming and outgoing electrons. In a strong external magnetic field, the electrons are confined to chiral quantum Hall edge channels. The current measured in the drain lead of the spectrometer is displayed in Fig. 1(b), as a function of emitter and detector energy. In addition to signals that arise when the filter energy of the detector quantum dot is tuned below the energy of the emitter quantum dot [triangles I and II in Fig. 1(b)],[1] anomalous signatures appear when the detector energy exceeds the emitter energy [triangles III and IV in Fig. 1(b)].

The central goal of this paper is to demonstrate, from first principles, that the spectroscopic response in III and IV in the ETH spectrometer detector current, in which the detection energy exceeds the emission energy, is a consequence of interactions between electrons in the spatially separated source lead and reservoir region of the device. We show that such interactions cause direct transfer of energy to the sample's

[1]The positive current along the edge of triangle II results from higher-lying states in the detector dot [15].

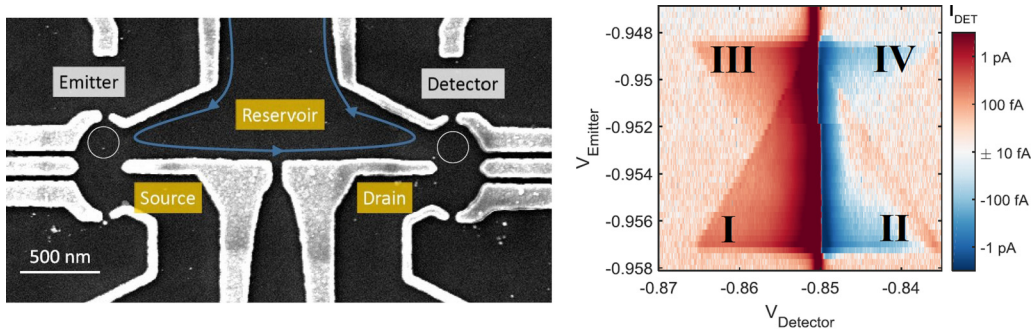

(a) sample micrograph (b) detector current

FIG. 1. (From Refs. [15,16]) (a) Mesoscopic sample for the spectral selection of charge carriers. Electrons from a source electrode are injected at a well-defined energy into a reservoir region via an emitter quantum dot. Subsequent energy selection at a detector quantum dot allows for the probing of intermediate relaxation of the electrons in the reservoir region. In the presence of a strong magnetic field, the electrons propagate along chiral quantum Hall edge channels (blue line). (b) Drain lead current of the sample displayed in (a) in a strong magnetic field, as a function of the voltages applied to emitter and detector quantum dot (note that emitter energies increase toward the bottom and detector energies increase toward the left). Depending on the detector quantum dot voltage, the energy introduced by electrons from the source electrode gives rise to either an electron current (red) or a hole current (blue) through the detector into the drain. Currents are also measured when the detector energy exceeds the emitter energy (relative to the reservoir chemical potential, triangles III and IV).

reservoir, that stems from Auger-type plasmon recombination processes in the source. These processes are enabled by source electrons recombining with holes that are left behind by electrons emitted into the reservoir. Our findings indicate that such processes may very well at least partly account for the unexpected energy loss reported in Refs. [10,14], which calls for controlling the relevant degrees of freedom in upcoming experimental setups, and for the consideration of such processes in further theoretical studies of energy relaxation. For our purpose, we need to take tunneling as well as interactions between the reservoir and source channel into account in our analysis. In addition, interactions within the sample's reservoir are considered, that account for the regular features I and II.

Theoretical models to capture mechanisms causing relaxation in edge channels often treat electron-electron interactions as a contact interaction, in a perturbative approach [12] or employing bosonization techniques. The inflow of electrons into the edge is described either by an initial nonequilibrium distribution in the channels [13,18] or by a perturbative [19–21] treatment of tunneling to noninteracting leads. Some studies have taken into account finite- or long-range interactions to describe either intrachannnel [13,22] or interchannel [13,23] relaxation, treating tunneling to leads perturbatively, or by considering an initial nonequilibrium distribution in the channels.

To relate distinct contributions observed in the spectrometer's detector current to specific interaction events and transfer processes, we employ a perturbative approach within the Keldysh nonequilibrium Green's function framework in a fermionic picture. The complexity of the diagrammatic approach, treating both interactions and tunneling simultaneously, rapidly increases with the perturbation order. To retain tractability, we consider second-order Coulomb interactions, which is the lowest order that captures relaxation. This corresponds to transition amplitudes, and thereby to physical processes, that involve the emission and absorption of one virtual photon. We limit our analysis to one channel per edge, considering finite-range interactions. This constitutes the minimal model to generate current in all triangles I to IV for second-order electron-electron interactions, and to thereby capture the experiment's essential features. Tunneling processes beyond one transmission event per quantum dot[2] can be neglected if tunnel coupling to the quantum dots is weak since these processes are typically suppressed by the ratio of the tunnel coupling strength to the intrinsic energy scales of the setup, such as the injection and detection energies as measured from the Fermi sea, or the energy of virtual photons. For finite-range interactions, processes in which two electrons pass one of the quantum dots consecutively are furthermore suppressed due to the Pauli principle, by the ratio of the screening length to the length of the spectrometer.[3]

The restriction to one-photon processes causes a truncation of the expression for the detector current in terms of spatial separation between emitter and detector quantum dots. Under the assumption that the spectrometer length exceeds the screening length, the probability of elastic processes, i.e., processes in which the emitted electron does not dissipate energy before entering the detector, decreases quadratically with the spatial separation of the quantum dots. The physical constraint that this probability be positive subsequently limits the validity of the perturbative approach in terms of a combination of admissible interaction strength, spectrometer and screening length, as well as energy of injected electrons. The corresponding probability of inelastic processes, in which a charge carrier is excited from the Fermi sea, simultaneously

[2]The term transmission event in this context corresponds to the probability of an electron tunneling through a quantum dot in an otherwise decoupled system.

[3]Coulomb interactions between electrons on the quantum dots and between electrons on the quantum dots and the channels are not taken into account. Such interactions would further suppress consecutive tunneling events due to Coulomb blockade.

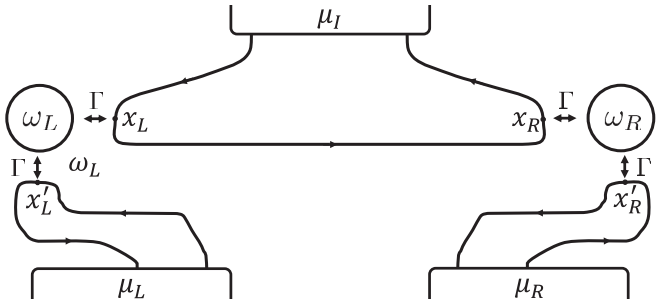

FIG. 2. Sketch of the experimental sample: source (L), drain (R), and reservoir region (I) channels are held at the chemical potentials μ_L, μ_R, and μ_I, respectively. The source and drain channels are coupled to the reservoir region via the emitter quantum dot at energy ω_L and the detector quantum dot at energy ω_R, with tunneling coupling strength Γ.

increases at the same rate.[4] Additional features of the detector current, that require going beyond second-order perturbation theory in interactions, are discussed in Sec. IX.

The description of the aforementioned Auger-type recombination processes in the source channel, depicted in Fig. 17, constitutes our central result. The diagrams which correspond to these processes in our perturbative approach, shown in Figs. 16 and 18, generate current exactly in triangles III and IV, as is apparent from Eqs. (55) and (57). Figure 19 furthermore shows the current generated in all triangles I to IV [compare Fig. 1(b)]. Figure 20 shows the evolution of the initial edge channel distribution for increasing spatial separation of the quantum dots.

The paper is structured as follows: In Sec. II, we introduce a model Hamiltonian to describe the ETH sample, devised to capture the distinct features of the current measured in the detector quantum dot. In Sec. III we develop a general expression for the detector current in terms of the Keldysh nonequilibrium Green's functions technique. In Sec. IV we solve our model for the case without interactions between charge carriers. In Sec. V we develop systematics in Keldysh space when interactions are taken into account. In Secs. VI and VII we introduce interaction terms within the reservoir, as well as between reservoir and source lead, respectively, before we evaluate the general expressions resulting from our approach for a finite-range model interaction in Sec. VIII.

II. MODEL AND ENERGY SCALES

In this section, we present a model devised to capture the individual contributions I to IV, displayed in Fig. 1(b), to the inelastic current measured in the electron spectrometer.

A sketch of the sample is shown in Fig. 2: the source channel to the left (L), the drain channel to the right (R), and the intermediate (I) reservoir channel are held at the chemical potentials μ_L, μ_R, and μ_I, respectively. Before interactions are considered, these channels are described as a one-dimensional chiral free-electron gas with linear dispersion relation. The spatial coordinate along the channels thereby runs from negative to positive infinity, where periodic boundary conditions are imposed, and effects of curvature are not taken into account. Note that we restrict the treatment to a single edge channel per region. The experimental data suggest that interactions are of sufficient range to enable intrachannel relaxation [13,22] to partially and qualitatively account for the signal in triangles I and II.

The source lead is tunnel coupled at position x'_L to the emitter quantum dot, described as a single resonant level ω_L. In the same way, the drain lead couples to the detector quantum dot ω_R at position x'_R. Both quantum dots are in turn coupled to the reservoir region at their respective positions x_L and x_R along the reservoir channel.

While it suffices to take into account interactions within the reservoir channel to generate triangles I and II, generation of triangles III and IV additionally requires accounting for interactions between the source and reservoir channels, as will be shown in Secs. VI and VII. The total Hamiltonian of the model is thus composed of three contributions:

$$H = H_0 + H_T + H_V. \tag{1}$$

H_0 contains the description of the individual parts of the system without tunneling or interactions,

$$H_0 = \sum_{\substack{\alpha=L,R \\ k_\alpha}} \epsilon_{k_\alpha} \hat{l}^\dagger_{k_\alpha} \hat{l}_{k_\alpha} + \sum_{\alpha=L,R} \omega_\alpha \hat{d}^\dagger_\alpha \hat{d}_\alpha + \sum_k \epsilon_k \hat{r}^\dagger_k \hat{r}_k. \tag{2}$$

Here, $\hat{l}_{k_\alpha}$ denote the fermionic annihilation operators of the left and right leads, $\hat{d}_\alpha$ of the left and right quantum dots, and $\hat{r}_k$ of the intermediate reservoir region. The tunneling Hamiltonian

$$H_T = \sum_{\substack{\alpha=L,R \\ k_\alpha}} \left[t_{k_\alpha \alpha} \hat{l}^\dagger_{k_\alpha} \hat{d}_\alpha + t^*_{k_\alpha \alpha} \hat{d}^\dagger_\alpha \hat{l}_{k_\alpha} \right] + \sum_{\substack{\alpha=L,R \\ k}} \left[t_{k\alpha} \hat{r}^\dagger_k \hat{d}_\alpha + t^*_{k\alpha} \hat{d}^\dagger_\alpha \hat{r}_k \right] \tag{3}$$

describes tunneling coupling between the lead channels and the dots, as well as between the dots and the reservoir region. The tunneling amplitudes $t_{k_\alpha \alpha} = t \exp(-ik_\alpha x'_\alpha)$ and $t_{k\alpha} = t \exp(-ikx_\alpha)$ contain the system's spatial information and describe the local coupling of the leads to the left and right dots at x'_L and x'_R, as well as the local coupling of the dots to the reservoir at x_L and x_R, respectively, $x_L < x_R$. The amplitudes t are assumed to be momentum independent and equal for all tunneling to the left and to the right quantum dot, and determine, in combination with the density of states ρ in the respective lead, the tunneling coupling strength $\Gamma = 2\pi |t|^2 \rho$. The interaction Hamiltonian

$$H_V = H_V\left(\{\hat{l}_{k_\alpha}, \hat{l}^\dagger_{k_\alpha}, \hat{r}_k, \hat{r}^\dagger_k\}\right) \tag{4}$$

generally depends on the lead and reservoir creation and annihilation operators in a way that will be specified when the respective interactions are accounted for in Secs. VI and VII.

Energy scales in the experiment are approximately $\Gamma \sim 1\ \mu\text{eV} < k_B T \sim 2.5\ \mu\text{eV} < \hbar v/\Delta x \sim 30\ \mu\text{eV} < \mu_L -$

[4]Processes encompassing more than one virtual photon eventually generate higher-order expressions in terms of spatial quantum dot separation.

$\mu_R \sim 400\ \mu\text{eV} - 1\ \text{m eV}$ [15], where T is the temperature of the sample. Due to the proximity of the top gates to the two-dimensional electron gas in the experiment (∼90 nm), as our main assumption, we estimate the screening length λ to be by an order of magnitude shorter than the distance between the quantum dots, $\lambda \ll \Delta x$. Calculations are performed at $T = 0$, which gives rise to an error whenever ω_L and ω_R are within a range of $k_B T$ to either chemical potential μ_L or μ_R for elastic transfer, or within a range of $k_B T$ to the outlines of triangles I to IV for inelastic transfer, as is illustrated in Sec. VI B 1.

III. GENERAL EXPRESSION FOR DRAIN LEAD CURRENT

The central observable in the electron spectrometer is the current through the drain lead. In this section, a general expression for this current is stated, which serves as the basis for all further considerations. Within the framework of the Keldysh nonequilibrium Green's function formalism, the goal is to express the current in terms of the full Green's functions of the reservoir region, containing both information about tunneling as well as about interactions, following the approach of Ref. [24].

The current through the drain lead is given by

$$\begin{aligned} I_R &= -e\langle \dot{n}_R(t)\rangle \\ &= -\frac{ie}{\hbar}\sum_{k_R}[t_{k_R R}\langle \hat{l}^\dagger_{k_R}(t) d_R(t)\rangle - t^*_{k_R R}\langle d^\dagger_R(t)\hat{l}_{k_R}(t)\rangle]. \end{aligned} \tag{5}$$

After Fourier transformation, we obtain

$$I_R = -\frac{e}{2\pi}\int_{-\infty}^{\infty} d\omega \sum_{k_R}\left[t_{k_R R} G^<_{R k_R}(\omega) - t^*_{k_R R} G^<_{k_R R}(\omega)\right], \tag{6}$$

where we used the definition of the lesser Green's function $G^<_{R k_R}(t,t) = i\langle \hat{l}^\dagger_{k_R}(t) d_R(t)\rangle/\hbar$ on the Keldysh contour.

In the following we set $\hbar = k_B = 1$ and adopt a matrix notation in which $\mathrm{D_{L/R}}$ denotes the index of the left/right quantum dot, $\mathrm{L_{L/R}}$ denotes the indices of the left/right lead, and I denotes the indices of the intermediate reservoir region. In this section, all Green's functions depend on the energy ω, which allows us to suppress this dependency in our notation. Thus, (6) is written as

$$I_R = -\frac{e}{2\pi}\int_{-\infty}^{\infty} d\omega\, \mathrm{tr}\left\{\mathbf{t}_{\mathrm{L_R D_R}}\mathbf{G}^<_{\mathrm{D_R L_R}} - \mathbf{G}^<_{\mathrm{L_R D_R}}\mathbf{t}_{\mathrm{D_R L_R}}\right\}. \tag{7}$$

Taking the detector quantum dot and the right lead to be noninteracting allows to recast (7) into the desired general form

$$\begin{aligned} I_R = -\frac{e}{2\pi}\int_{-\infty}^{\infty} d\omega\, \mathrm{tr}\big\{&\bar{\mathbf{g}}^a_{\mathrm{D_R D_R}}\boldsymbol{\Sigma}^<_{\mathrm{D_R L_R D_R}}\bar{\mathbf{g}}^r_{\mathrm{D_R D_R}}\boldsymbol{\Sigma}^>_{\mathrm{D_R I D_R}} \\ &- \bar{\mathbf{g}}^a_{\mathrm{D_R D_R}}\boldsymbol{\Sigma}^>_{\mathrm{D_R L_R D_R}}\bar{\mathbf{g}}^r_{\mathrm{D_R D_R}}\boldsymbol{\Sigma}^<_{\mathrm{D_R I D_R}}\big\}, \end{aligned} \tag{8}$$

as is shown in Appendix A. In (8),

$$\bar{\mathbf{g}}_{\mathrm{D_R D_R}} = \mathbf{g}_{\mathrm{D_R D_R}} + \mathbf{g}_{\mathrm{D_R D_R}}\boldsymbol{\Sigma}_{\mathrm{D_R L_R D_R}}\bar{\mathbf{g}}_{\mathrm{D_R D_R}} \tag{9}$$

describes charge carriers passing back and forth between the detector dot and the right lead, where

$$\boldsymbol{\Sigma}_{\mathrm{D_R L_R D_R}} = \mathbf{t}_{\mathrm{D_R L_R}}\mathbf{g}_{\mathrm{L_R L_R}}\mathbf{t}_{\mathrm{L_R D_R}} \tag{10}$$

denotes the tunneling self-energy of the isolated drain lead. The tunneling self-energy of the interacting reservoir region

$$\boldsymbol{\Sigma}_{\mathrm{D_R I D_R}} = \mathbf{t}_{\mathrm{D_R I}}\mathbf{G}_{\mathrm{II}}\mathbf{t}_{\mathrm{I D_R}} \tag{11}$$

contains the Green's function of the reservoir region $\mathbf{G}_{\mathrm{II}}$ which develops with the total Hamiltonian H. In the following sections, this Green's function will be evaluated for different types of interactions, and determines the drain current.

Written explicitly, the general expression for the current (8) reads

$$\begin{aligned} I_R = -\frac{ie}{2\pi}\int_{-\infty}^{\infty} d\omega\, A_{\mathrm{D_R}}(\omega)\sum_{k,k'}&[f_R(\omega) t_{Rk} G^>_{kk'}(\omega) t_{k'R} \\ &- [f_R(\omega) - 1] t_{Rk} G^<_{kk'}(\omega) t_{k'R}]. \end{aligned} \tag{12}$$

Here,

$$A_{\mathrm{D_R}}(\omega) = \frac{\Gamma(\omega)}{(\omega - \omega_R)^2 + \frac{\Gamma(\omega)^2}{4}} \tag{13}$$

reflects the broadening of the detector quantum dot's energy level due to the coupling to the drain lead.[5] The occupation of the drain lead is described by the Fermi distribution f_R, and the tunneling coupling strength $\Gamma(\omega)$ is here determined by the density of states $\rho(\omega)$ in the drain lead.

IV. NONINTERACTING CASE

In this section, we solve the noninteracting case, setting $H_V \equiv 0$. We treat the intermediate reservoir region as a one-dimensional chiral channel with right-moving particles and linear dispersion relation, such that $\epsilon_k = vk$ in (2), where v is the channel's Fermi velocity.

In this case, the Green's function of the reservoir region develops according to the Dyson equation

$$\mathbf{G}^T_{\mathrm{II}} = \mathbf{g}_{\mathrm{II}} + \mathbf{g}_{\mathrm{II}}\boldsymbol{\Sigma}_{\mathrm{ITI}}\mathbf{G}^T_{\mathrm{II}}, \tag{14}$$

with the tunneling self-energy

$$\boldsymbol{\Sigma}_{\mathrm{ITI}} = \boldsymbol{\Sigma}_{\mathrm{ID_L I}} + \boldsymbol{\Sigma}_{\mathrm{ID_R I}}, \tag{15}$$

in which

$$\boldsymbol{\Sigma}_{\mathrm{ID_{L/R} I}} = \mathbf{t}_{\mathrm{ID_{L/R}}}\bar{\mathbf{g}}_{\mathrm{D_{L/R} D_{L/R}}}\mathbf{t}_{\mathrm{D_{L/R} I}}. \tag{16}$$

The superscript T in (14) indicates that these Green's functions of the intermediate region develop without interaction terms.

The kinetic equation for the lesser component of (14) reads

$$\begin{aligned} \mathbf{G}^{T<}_{\mathrm{II}} = &\left(\mathbf{I} + \mathbf{G}^{Tr}_{\mathrm{II}}\boldsymbol{\Sigma}^r_{\mathrm{ITI}}\right)\mathbf{g}^<_{\mathrm{II}}\left(\mathbf{I} + \boldsymbol{\Sigma}^a_{\mathrm{ITI}}\mathbf{G}^{Ta}_{\mathrm{II}}\right) \\ &+ \mathbf{G}^{Tr}_{\mathrm{II}}\boldsymbol{\Sigma}^<_{\mathrm{ITI}}\mathbf{G}^{Ta}_{\mathrm{II}}, \end{aligned} \tag{17}$$

with "$<\to>$" for the greater component. Here, the superscripts r and a denote the retarded and advanced components of the respective Green's functions. Upon insertion into (8), the first term of (17) gives rise to a current exchanged directly between the intermediate reservoir and the drain lead which depends on the respective chemical potentials of those regions

[5] Taking into account also the broadening by the coupling to the reservoir generates the transition coefficient (19).

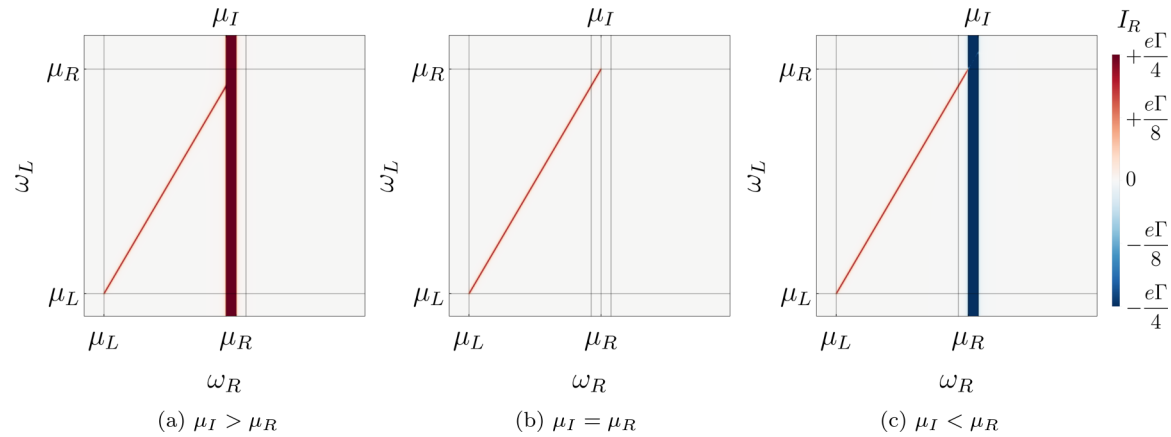

FIG. 3. Current (21) through drain in absence of interactions, for large bias between source and drain channels, and for (a) slightly positive, (b) zero, and (c) slightly negative bias between reservoir and drain channels. Note that dot energies increase from top to bottom and from right to left and that the aspect ratio has been adjusted, so as to match the conventions used in the experimental data shown in Fig. 1(b). [Parameters are $\mu_L = \mu_R + 400\Gamma$, $\mu_I =$ (a): $\mu_R + 30\Gamma$, (b): μ_R, (c): $\mu_R - 30\Gamma$.]

μ_I and μ_R. The second term of (17) gives rise to a current depending on the chemical potentials μ_L and μ_R of the source and the drain leads. Evaluation of the respective transition self-energies is presented in Appendix B.

The explicit expression for the current of the noninteracting system then reads

$$I_R = \frac{e}{2\pi}\int_{-\infty}^{\infty} d\omega [f_I(\omega) - f_R(\omega)]\mathcal{R}_L(\omega)\mathcal{T}_R(\omega) + \frac{e}{2\pi}\int_{-\infty}^{\infty} d\omega [f_L(\omega) - f_R(\omega)]\mathcal{T}_L(\omega)\mathcal{T}_R(\omega), \tag{18}$$

with transmission coefficient

$$\mathcal{T}_{L/R}(\omega) = \frac{\Gamma(\omega)^2}{(\omega - \omega_{L/R})^2 + \Gamma(\omega)^2} \tag{19}$$

and reflection coefficient

$$\mathcal{R}_{L/R}(\omega) = 1 - \mathcal{T}_{L/R}(\omega). \tag{20}$$

Since no interactions between electrons have been considered so far, the explicit formula for the current through the drain lead (18) coincides with the Landauer-Büttiker result [24]. The first line in (18), which describes current exchanged directly between the reservoir region and the drain, shows that charge carriers provided by the reservoir must be reflected at the emitter quantum dot before they can be transmitted through the detector (see Fig. 2). The second line in (18) requires transmission through both quantum dots at the same energy, and therefore constitutes the contribution of elastically transferred electrons.

At zero temperature and for constant density of states in the source, drain, and reservoir regions, i.e., constant Γ, (18) is given by

$$I_R = \frac{e\Gamma}{2\pi}[\arg(\omega_R - \mu_I + i\Gamma) - \arg(\omega_R - \mu_R + i\Gamma)] - I_{\rm el}(\mu_I, \mu_R) + I_{\rm el}(\mu_L, \mu_R), \tag{21}$$

where for the elastic current transmitted through both dots, which corresponds to the second line of (18), we have

$$I_{\rm el}(\mu_L, \mu_R) = \frac{e\Gamma}{2\pi}\frac{\Gamma^2}{(\omega_L - \omega_R)^2 + (2\Gamma)^2}\Bigg\{\arg(\omega_L - \mu_L + i\Gamma) - \arg(\omega_L - \mu_R + i\Gamma) + \arg(\omega_R - \mu_L + i\Gamma) - \arg(\omega_R - \mu_R + i\Gamma) + \frac{\Gamma}{\omega_L - \omega_R}\log\left[\frac{((\omega_L - \mu_R)^2 + \Gamma^2)((\omega_R - \mu_L)^2 + \Gamma^2)}{((\omega_L - \mu_L)^2 + \Gamma^2)((\omega_R - \mu_R)^2 + \Gamma^2)}\right]\Bigg\}. \tag{22}$$

The current (21) is displayed in Fig. 3, for large bias between source and drain leads, and for [Fig. 3(a)] slightly positive, [Fig. 3(b)] zero, and [Fig. 3(c)] slightly negative bias between reservoir and drain leads.

V. GREEN'S FUNCTIONS IN THE PRESENCE OF INTERACTIONS

In this section, a systematic scheme to develop the contour-ordered Green's functions is presented, for the case in which interactions within the reservoir region are considered.

The central object to determine the current through the drain lead, (8) and (12), are the lesser and greater Green's functions of the reservoir region, governed by the total Hamiltonian H, for which we have the kinetic equation

$$\mathbf{G}^<_{\rm II} = (\mathbf{I} + \mathbf{G}^r_{\rm II}\mathbf{\Sigma}^r_{\rm II})\mathbf{g}^<_{\rm II}(\mathbf{I} + \mathbf{\Sigma}^a_{\rm II}\mathbf{G}^a_{\rm II}) + \mathbf{G}^r_{\rm II}\mathbf{\Sigma}^<_{\rm II}\mathbf{G}^a_{\rm II}, \tag{23}$$

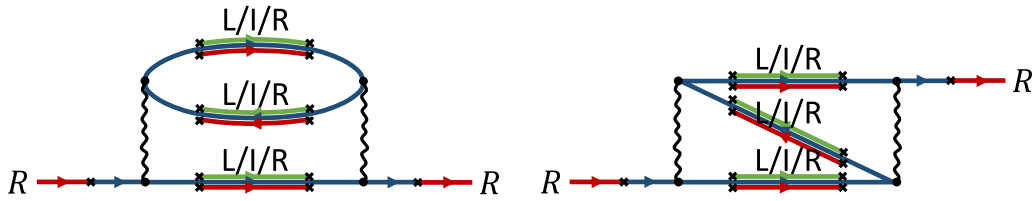

(a) Tunneling-dressed polarization diagram (b) Tunneling-dressed exchange diagram

FIG. 4. Tunneling-dressed (a) polarization and (b) exchange self-energy diagrams. Diagrams that determine the current through the drain are terminated by Green's functions of this channel (red lines). Tunneling (black crosses) from the intermediate region (blue lines) to the source (green lines) and drain channels through emitter and detector quantum dot, respectively, generates 27 diagrams for both self-energies. These 27 diagrams correspond to 27 distinct physical processes. Limiting tunneling as described in Sec. VI, only three of those processes remain.

with the replacement "$<\rightarrow>$" for the greater component. Since Green's functions and self-energies in (23) depend both on tunneling and interaction Hamiltonians H_T and H_V, respectively, a method to separate those dependencies is desirable.

In a diagrammatic expansion of Green's functions which include both these types of processes, it is possible to rearrange terms such that each interaction event is succeeded by all possible tunneling events, before the next interaction event is considered. This leads to the Dyson equation

$$\mathbf{G}_{\mathrm{II}} = \mathbf{G}^T_{\mathrm{II}} + \mathbf{G}^T_{\mathrm{II}}\boldsymbol{\Sigma}_{\mathrm{IVI}}\mathbf{G}_{\mathrm{II}} \tag{24}$$

for the Green's function of the reservoir region. Here, the tunneling Green's function $\mathbf{G}^T_{\mathrm{II}}$, previously encountered in (14), develops only with the tunneling self-energy, and all bare Green's function lines $\mathbf{g}_{\mathrm{II}}$ in the usual interacting self-energy without tunneling are replaced by $\mathbf{G}^T_{\mathrm{II}}$. This prescription defines the self-energy $\boldsymbol{\Sigma}_{\mathrm{IVI}}$.

In a next step, the Dyson equation (24) is truncated after the first iteration, i.e.,

$$\mathbf{G}_{\mathrm{II}} \simeq \mathbf{G}^T_{\mathrm{II}} + \mathbf{G}^T_{\mathrm{II}}\boldsymbol{\Sigma}_{\mathrm{IVI}}\mathbf{G}^T_{\mathrm{II}}, \tag{25}$$

which allows us to take into account the second order of interactions in the interacting self-energy $\boldsymbol{\Sigma}_{\mathrm{IVI}}$ in Sec. VI. Applying the Langreth rules to (25), we find

$$\begin{aligned}\mathbf{G}^<_{\mathrm{II}} \simeq\ & \mathbf{G}^{T<}_{\mathrm{II}} + \mathbf{G}^{T<}_{\mathrm{II}}\boldsymbol{\Sigma}^a_{\mathrm{IVI}}\mathbf{G}^{Ta}_{\mathrm{II}} \\ & + \mathbf{G}^{Tr}_{\mathrm{II}}\boldsymbol{\Sigma}^<_{\mathrm{IVI}}\mathbf{G}^{Ta}_{\mathrm{II}} + \mathbf{G}^{Tr}_{\mathrm{II}}\boldsymbol{\Sigma}^r_{\mathrm{IVI}}\mathbf{G}^{T<}_{\mathrm{II}},\end{aligned} \tag{26}$$

with "$<\rightarrow>$" for the greater component of the Green's function. The first term in (26) gives rise to the noninteracting current of Sec. IV. The second and fourth terms in (26) constitute corrections to this current due to the interaction term. This follows from the fact that the lesser tunneling Green's functions (and the greater tunneling Green's functions of the corresponding expression) in (26) are evaluated at the same energy ω as the lesser and greater Green's function of the drain lead, which enter the general formula of the current (8) via the corresponding tunneling self-energies $\boldsymbol{\Sigma}^{</>}_{\mathrm{D_R L_R D_R}}$. Thereby, the current generated by the latter terms is confined to the same regions in the ω_L/ω_R space as the elastic current shown in Fig. 3.

The third term in (26) gives rise to inelastic contributions to the current since the lesser/greater interacting self-energies entail equilibration at energies different from ω, as is demonstrated in the following section.

VI. INTERACTIONS IN THE RESERVOIR REGION

In this section, Coulomb interaction between electrons in the reservoir region is explicitly taken into account. The interaction is described by the Hamiltonian

$$H^I_V = \frac{1}{2\Omega}\sum_{k,k',q} v_q \hat{r}^\dagger_{k-q}\hat{r}^\dagger_{k'+q}\hat{r}_{k'}\hat{r}_k, \tag{27}$$

where

$$v_q = \int_{-\infty}^{\infty} dr\, \gamma_r e^{iqr} \tag{28}$$

is the Fourier transform of the Coulomb matrix element γ_r in real space. In a diagrammatic approach, the first-order Hartree and Fock contributions contain divergent terms, which have been shown via a bosonization calculation to correspond to a mere shift of the chemical potential [25]. The converging part of the exchange contribution additionally gives rise to a momentum-dependent renormalization of velocities, which saturates above $1/\lambda$. Below this value, second-order diagrams largely cancel. In Keldysh space, the first-order contributions act in the same way as one-body potentials, and therefore do not give rise to inelastic processes.[6] Thus, we neglect these contributions, and exclusively consider the polarization and exchange diagrams in the interacting self-energy, which are the lowest-order diagrams generating inelastic current. The tunneling-dressed versions of these diagrams, which correspond to the third term of (26), are displayed in Fig. 4.

In the following, we consider equal chemical potentials in the reservoir and drain lead regions $\mu_I = \mu_R$. We consider one transmission event per quantum dot, i.e., we collect all tunneling amplitudes which combine to the product $\mathcal{T}_L\mathcal{T}_R$ [cf. (19)], discarding further tunneling processes. In this way, we disregard processes in which more than one electron passes through the same quantum dot. For contact interactions, such processes are precluded by the Pauli exclusion principle since in this case the emitted electron and excited electrons arrive at the detector at the same time. Explicit evaluation of such processes for finite-range interactions shows that the approximation is justified as long as the screening length is

[6] In Keldysh space, one-body potentials only affect retarded and advanced self-energies. The greater and lesser components of the self-energy are unaffected [26]. Only the latter cause inelastic currents.

smaller than the dot separation $\lambda \ll \Delta x$. The approximation overestimates currents within a range of Γ of the lines of zero-momentum transfer, i.e., the hypotenuses of triangles I to IV, for inelastic transfer. Furthermore, processes in which the initial source electron returns into the emitter quantum dot after interacting with electrons in the reservoir are neglected.

A. Corrections to elastic current

The interaction corrections to the elastic current are the second and fourth terms in expansion (26). The explicit expression for the correction in terms of Green's functions is contained in Appendix C 1.

After collection of those tunneling amplitudes which combine to the product of the transition probability through the left and the right dot (19), evaluation of the correction terms requires the retarded and advanced components of the self-energy $\mathbf{\Sigma}_{\mathrm{IVI}}$ to zeroth order in tunneling amplitudes, denoted by Σ. These components are obtained from the respective lesser/greater elements[7] upon employing the Kramers-Kronig relation

$$\mathbf{G}^{r/a}(\omega) = \frac{i}{2\pi}\int_{-\infty}^{\infty} d\omega' \frac{\mathbf{G}^{>}(\omega') - \mathbf{G}^{<}(\omega')}{\omega - \omega' \pm i\delta}. \tag{29}$$

The matrix elements are given by

$$\Sigma_k(\omega)^{r/a} = g_k^{r/a}(\omega)E^2(vk). \tag{30}$$

Here, we have defined $E^2 = E^2_{\mathrm{pol}} + E^2_{\mathrm{exch}}$ to which, at zero temperature, the polarization diagram contributes (see also Ref. [25]) with

$$E^2_{\mathrm{pol}}(\omega) = \frac{1}{(2\pi v)^2}\int_0^{\mu_I-\omega} d\omega'\, \omega' v^2_{\omega'/v}, \tag{31}$$

and the exchange diagram contributes

$$E^2_{\mathrm{exch}}(\omega) = \frac{1}{(2\pi v)^2}\int_0^{\mu_I-\omega} d\omega''\, v_{\omega''/v}\int_{\mu_I-\omega-\omega''}^{\mu_I-\omega} d\omega'\, v_{\omega'/v}. \tag{32}$$

For E^2 decaying sufficiently fast as $\omega \to \infty$ in the complex plane, and upon neglecting poles of E^2, which holds for $\lambda \ll \Delta x$, the corrected elastic current becomes

$$I_R^{\mathrm{el,corr}} = \frac{e}{2\pi}\int_{-\infty}^{\infty} d\omega [f_L(\omega) - f_R(\omega)]\mathcal{T}_L(\omega)\mathcal{T}_R(\omega) \times\left[1 - \frac{\Delta x^2}{v^2}E^2(\omega) + \frac{\partial^2}{\partial\omega^2}E^2(\omega)\right] \tag{33}$$

(cf. Appendix C 1). The corrected current changes direction when the brackets in the second line of (33) take on negative values, rendering the present approximation unphysical at corresponding parameter values.[8] The approach is thus constrained by the condition[9]

$$\frac{\Delta x^2}{v^2}E^2(\omega) - \frac{\partial^2}{\partial\omega^2}E^2(\omega) \lesssim 1. \tag{34}$$

A plot of the corrected elastic current (33) is shown in Fig. 5 for the screened finite-range interaction

$$v_q = \frac{v_0}{1+\lambda^2 q^2}, \tag{35}$$

with constant v_0 and screening length λ. The poles of (35) are located at $q = \pm i/\lambda$ such that their contribution to the elastic correction is suppressed by $\exp(-\Delta x/\lambda)$ [cf. (C5)].[10] Approximation (33) is thus valid as long as $\lambda \ll \Delta x$. Under this assumption, for (35), as well as for qualitatively similar screened interactions, condition (34) imposes restrictions on admissible values for interaction strength, dot separation, screening length, as well as injection energy. With (35), for $(\omega - \mu_R) \ll v/\lambda$, (34), e.g., turns into $(v_0/2\pi v)^2(\Delta x/\lambda)^2[\lambda(\omega-\mu_R)/v]^6 11/180 \lesssim 1$, where ω corresponds to either dot level ω_R or ω_L. Corrections due to interactions cause the elastic current to diminish as the injection and detection energies increase from the Fermi level.

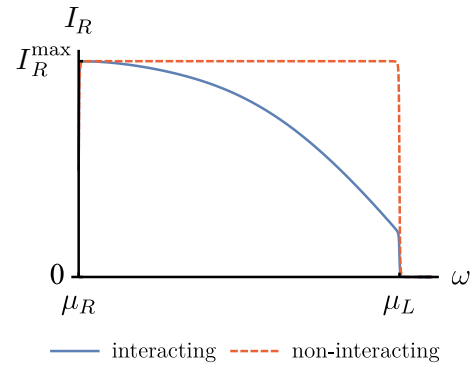

FIG. 5. Corrections due to interactions between electrons cause the elastic current (33) to decrease from the maximum value $I_R^{\max}$ as the distance $\omega = \omega_R = \omega_L$ of emitter and detector quantum dot energies is increased from the Fermi level μ_R. Elastic current close to zero indicates parameter values for which the perturbative approach to second order in interactions becomes unphysical [cf. (33) and (34)]. [Plot includes (31), (32), and interchannel correction (51), parameters are $\mu_L = \mu_R + 400\Gamma$, $v = 260\lambda\Gamma$, $v_0 = 640\lambda\Gamma$, $\Delta x = 8\lambda$, $d = 2.8\lambda$.]

B. Inelastic contributions

Inelastic contributions to the current are determined by the third term of expansion (26) of the lesser and greater reservoir Green's function on the Keldysh contour. According to the Langreth rules, each of the electron lines in Fig. 4 of the lesser self-energies in (26) corresponds to a lesser component Green's function, while the hole line corresponds to a greater

[7] The lesser and greater components on the Keldysh contour follow from the Langreth rules [27].

[8] At the present level, interaction corrections stem from the first term of the full Dyson series of interaction terms for nonlocal self-energies. Summing the respective full series leads to an exclusively positive oscillatory result. Inclusion of these higher-order terms requires a more sophisticated scheme to develop the reservoir region Green's function than provided by (25), which will be presented elsewhere.

[9] It has been demonstrated that, under these conditions, the relevant Green's function obtained from second-order perturbation theory agrees with the exact Green's function from bosonization [25].

[10] Terms that show an oscillatory dependence on $\omega\Delta x/v$ are therefore exponentially suppressed in $\Delta x/\lambda$ [cf. also (E1)].

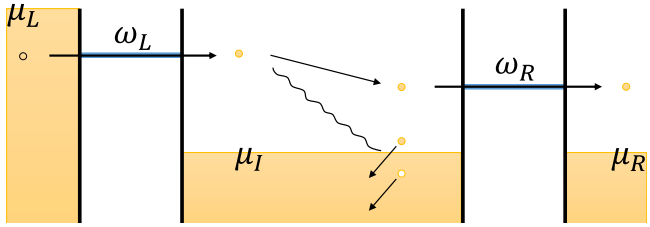

(a) Direct electron current process

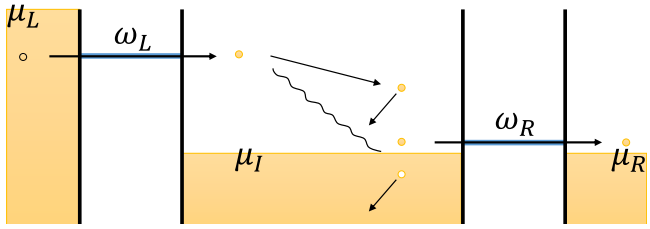

(b) Electron swap process

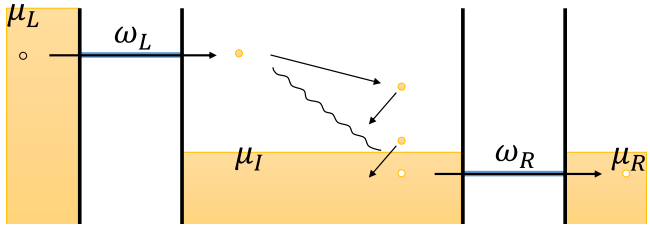

(c) Hole current process

FIG. 6. Introducing interactions within the reservoir channel of the sample, three second-order processes contribute to the inelastic current: (a) In the first process, an incoming electron generates an electron-hole pair, and subsequently enters the detector quantum dot at a lower energy. (b) In the second process, the electron of the pair enters the detector, while the initial electron equilibrates in the reservoir region. Due to indistinguishability of the electrons, processes (a) and (b) interfere. (c) In the third process, the hole of the pair can escape into the detector when the latter's energy is tuned below the Fermi level.

component Green's function. For the greater self-energies, the opposite relations hold. Each of these lesser/greater tunneling Green's functions

$$\mathbf{G}^{T\,</>}_{\mathrm{II}} = \left(\mathbf{I} + \mathbf{G}^{Tr}_{\mathrm{II}}\boldsymbol{\Sigma}^{r}_{\mathrm{ITI}}\right)\mathbf{g}^{</>}_{\mathrm{II}}\left(\mathbf{I} + \boldsymbol{\Sigma}^{a}_{\mathrm{ITI}}\mathbf{G}^{Ta}_{\mathrm{II}}\right) + \mathbf{G}^{Tr}_{\mathrm{II}}\boldsymbol{\Sigma}^{</>}_{\mathrm{ID_LI}}\mathbf{G}^{Ta}_{\mathrm{II}} + \mathbf{G}^{Tr}_{\mathrm{II}}\boldsymbol{\Sigma}^{</>}_{\mathrm{ID_RI}}\mathbf{G}^{Ta}_{\mathrm{II}} \tag{36}$$

allows for equilibration in all of the setup's channels: while the first term in (36) corresponds to equilibration in the reservoir itself (middle blue lines in Fig. 4), the second and third terms are associated with equilibration in the source (green lines) and drain (red lines) leads, respectively. Thereby, both diagrams in Fig. 4 are related to 27 distinct relaxation processes.

These processes are revealed upon dividing the diagrams at the innermost Green's function lines (see, e.g., Fig. 7). While the polarization diagrams are related to the probability of the individual processes (here the left half of each diagram corresponds to the complex conjugate of the respective right half), the exchange diagrams are related to interference terms due to indistinguishability of the electrons involved in these

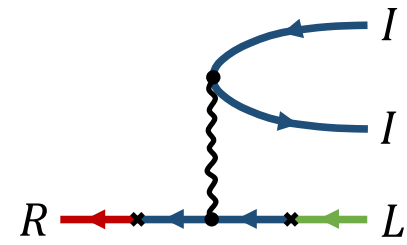

FIG. 7. Diagram corresponding to the amplitude of the inelastic process depicted in Fig. 6(a). This process gives rise to contribution (42) to the current through the drain channel.

processes. The diagrams are terminated by drain lines since the current in this channel is calculated.

Diagrams are evaluated at zero temperature $T = 0$, for equal chemical potentials in the reservoir and drain regions $\mu_I = \mu_R$, and for delta-function energy filter quantum dots, i.e., upon invoking the approximation

$$\mathcal{T}_{L/R}(\omega) = \frac{\Gamma^2}{(\omega - \omega_{L/R})^2 + \Gamma^2} \simeq \pi\Gamma\delta(\omega - \omega_{L/R}). \tag{37}$$

Taking into account only one charge carrier transfer process per quantum dot, as described in the last paragraph of Sec. VI, 3 of the 27 possible processes remain. In the remainder of the section, these processes will be evaluated.

1. Direct electron current process, polarization diagram

The first inelastic process considered is shown in the diagram in Fig. 7. The dynamics which corresponds to this diagram is depicted in Fig. 6(a): an electron from the source lead enters through the emitter quantum dot into the reservoir region. In the reservoir region, this electron dissipates energy upon creation of an electron-hole pair. While the initial electron is transmitted through the detector dot into the drain lead, the electron and hole of the pair equilibrate in the reservoir region.

The current generated by the diagram expressed in terms of Keldysh Green's functions (C7) is contained in Appendix C 2. Collecting tunneling amplitudes which combine to the product of the transition probabilities $\mathcal{T}_L$ and $\mathcal{T}_R$ through the left and right dots at energies $\omega + \omega''$ and ω, respectively, this contribution becomes

$$I^{1a}_R = -\frac{e}{(2\pi)^3}\int_{-\infty}^{\infty}d\omega''\int_{-\infty}^{\infty}d\omega'\int_{-\infty}^{\infty}d\omega\mathcal{T}_L(\omega+\omega'')\mathcal{T}_R(\omega) \times [f_R(\omega)[f_L(\omega+\omega'')-1]f_I(\omega'+\omega'')[f_I(\omega')-1] - \text{“}f \leftrightarrow (f-1)\text{”}]|\Upsilon(\omega'')|^2, \tag{38}$$

where

$$\Upsilon(\omega'') = -\frac{v_{\omega''/v}}{2\pi}\int_{-\infty}^{\infty}dk\frac{\exp\left(i\frac{\Delta x}{v}(vk-\omega)\right)}{(vk-\omega-i\delta)^2} = \frac{v_{\omega''/v}}{v}\frac{\Delta x}{v}. \tag{39}$$

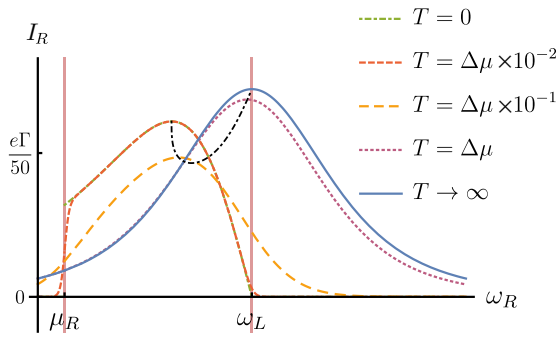

FIG. 8. Temperature dependence of inelastic contribution (40), stemming from the process depicted in Fig. 6(a), at fixed emitter energy. At temperatures comparable to the experimental value (red dashed line), the current is in good agreement with its value at $T = 0$ (green dashed-dotted line), except within a range of T to triangle outline (42). The black dashed-dotted line indicates the maximum of the current as T is varied between 0 and ∞. (Parameters are $\mu_L = \mu_R + 400\Gamma$, $\omega_L = \mu_R + 350\Gamma$, $v = 260\lambda\Gamma$, $v_0 = 720\lambda\Gamma$, $x = 8\lambda$.)

For delta-like filters (37) and $\mu_I = \mu_R$, inelastic contribution (38) turns into

$$I_R^{1a} = \frac{e}{2\pi}\frac{\Gamma^2}{4}(\omega_L - \omega_R)|\Upsilon(\omega_L - \omega_R)|^2 \times \frac{1}{4}\mathrm{csch}\left[\frac{\beta}{2}(\omega_L - \omega_R)\right]\mathrm{sech}\left[\frac{\beta}{2}(\mu_L - \omega_L)\right] \times \mathrm{sech}\left[\frac{\beta}{2}(\mu_R - \omega_R)\right]\sinh\left[\frac{\beta}{2}(\mu_L - \mu_R)\right]. \quad (40)$$

For infinite temperature, (40) becomes

$$I_R^{1a} = \frac{e}{2\pi}\frac{\Gamma^2}{4}\frac{\mu_L - \mu_R}{4}|\Upsilon(\omega_L - \omega_R)|^2, \quad (41)$$

whereas at zero temperature we find

$$I_R^{1a} = \frac{e}{2\pi}\frac{\Gamma^2}{4}(\omega_L - \omega_R)|\Upsilon(\omega_L - \omega_R)|^2 \times [\theta(\mu_R - \omega_R) - \theta(\mu_L - \omega_R)] \times [\theta(\omega_R - \omega_L) - \theta(\mu_L - \omega_L)]. \quad (42)$$

The first line of (42) contains spatial and energetic dependencies of the current. The second line of (42) describes the outline of triangle I in Fig. 1(b), in the emitter-detector energy space.

Figure 8 shows the current (40) at given bias $\Delta\mu = \mu_L - \mu_R$ and emitter energy ω_L for several values of the temperature, for the model interaction (35). At temperatures comparable to the experimental value, $T = \Delta\mu \times 10^{-2}$ (red line), except within a range of T to the outline of triangle I, the current is in good agreement with its value for zero temperature (green line). All following diagrams are thus evaluated at $T = 0$. At infinite temperature (blue line), the current is proportional to the bias $\Delta\mu$, and its emitter-detector energy dependence is completely determined by the form of the interaction [cf. (39) and (41)].

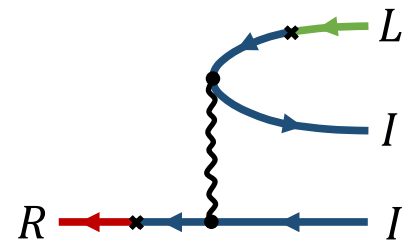

FIG. 9. Diagram corresponding to the process depicted in Fig. 6(b), in which the source electron is swapped for an electron from the Fermi sea, subsequently entering the detector quantum dot.

2. *Electron swap process, polarization diagram*

The contribution of the second inelastic process is determined by the diagram displayed in Fig. 9. In contrast to the previous physical process considered in Fig. 6(a), here the electron of the electron-hole pair generated in the reservoir region enters the detector quantum dot, as depicted in Fig. 6(b). Since the involved electrons are indistinguishable, the two processes interfere. The information about this interference is contained in the diagrams of the exchange self-energy, as will become apparent in Sec. VI B 4.

Analogously to Sec. VI B 1, the contribution of the diagram to the current, expressed in terms of Keldysh Green's functions (C8), turns into

$$I_R^{1b} = \frac{e}{2\pi}\frac{\Gamma^2}{4}\int_{\mu_I - \omega_L}^{\mu_I - \omega_R} d\omega'' \, |\Xi(\omega'')|^2 \times [\theta(\mu_R - \omega_L) - \theta(\mu_L - \omega_L)] \times [\theta(\mu_R - \omega_R) - \theta(\omega_L - \omega_R)], \quad (43)$$

where

$$\Xi(\omega'') = -\frac{1}{2\pi}\int_{-\infty}^{\infty} dq \, v_q \frac{\exp\left(i\frac{\Delta x}{v}(vq - \omega'')\right)}{(vq - \omega'' - i\delta)^2}. \quad (44)$$

The second line in (43) once again marks the outline of triangle I in Fig. 1(b).[11]

[11]The combinations of θ functions in (42) and (43) can be transformed into one another upon repeated application of $\theta(x - a)\theta(b - x) = \theta(b - a)[\theta(b - x) - \theta(a - x)]$.

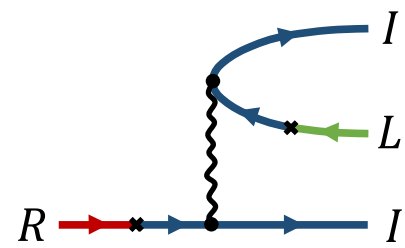

FIG. 10. Diagram corresponding to the process in Fig. 6(c), in which the hole of the electron-hole pair that is generated by the source electron escapes into the detector quantum dot.

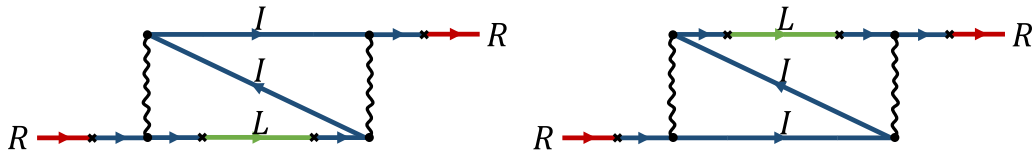

FIG. 11. The exchange diagrams for the electron current are obtained upon combining the process diagrams in Figs. 7 and 9. The diagrams describe interference of these processes.

3. Hole current process, polarization diagram

The third inelastic contribution is described by the diagram displayed in Fig. 10. The corresponding physical process is depicted in Fig. 6(c). In this process, the hole of the electron-hole pair, generated by the source electron, can tunnel into the detector quantum dot when the latter's resonant level is tuned below the Fermi sea. Thereby, a current of the opposite sign compared to the previously considered inelastic contributions is generated.

Similarly to the processes in Secs. VI B 1 and VI B 2, the Keldysh Green's function expression (C9) simplifies to

$$I_R^{1c} = -\frac{e}{2\pi}\frac{\Gamma^2}{4}\int_{\mu_I-\omega_R}^{\omega_L-\mu_I} d\omega''\,|\Xi(\omega'')|^2 \times [\theta(\mu_R-\omega_R)-\theta(2\mu_I-\mu_L-\omega_R)] \times [\theta(\mu_L-\omega_L)-\theta(2\mu_I-\omega_R-\omega_L)]. \quad (45)$$

The second and third lines of (45) in this case confine the current to triangle II in Fig. 1(b). As a function of the detector energy ω_R, contribution (45) constitutes the point reflection of (43) at the chemical potential μ_R.

4. Direct and swap electron processes, exchange diagram

The exchange diagrams of direct and swap electron processes are shown in Fig. 11. The diagrams can be obtained by joining the diagram halves in Figs. 7 and 9 by matching respective Green's function lines, which indicates that the exchange diagrams correspond to interference of the corresponding processes, as is confirmed by evaluation of the expressions below.

The diagrams constitute the complex conjugate of one another, so it is sufficient to determine the contribution of the diagram in Fig. 11(a). After employing the same approximations as in the previous diagrams to the Keldysh Green's functions (C10), the contribution simplifies to

$$I_R^{2a} = -\frac{e}{2\pi}\frac{\Gamma^2}{4}\Upsilon(\omega_L-\omega_R)\int_{\mu_I-\omega_L}^{\mu_I-\omega_R} d\omega''\,\Xi^*(\omega'') \times [\theta(\mu_R-\omega_R)-\theta(\mu_L-\omega_R)] \times [\theta(\omega_R-\omega_L)-\theta(\mu_L-\omega_L)]. \quad (46)$$

For completeness, we also state the corresponding expression for the diagram in Fig. 11(b):

$$I_R^{2b} = -\frac{e}{2\pi}\frac{\Gamma^2}{4}\Upsilon^*(\omega_L-\omega_R)\int_{\mu_I-\omega_L}^{\mu_I-\omega_R} d\omega''\,\Xi(\omega'') \times [\theta(\mu_R-\omega_R)-\theta(\mu_L-\omega_R)] \times [\theta(\omega_R-\omega_L)-\theta(\mu_L-\omega_L)]. \quad (47)$$

From the explicit expressions at given energies, it is apparent that (46) and (47) correspond to the interference terms of the processes generating (42) and (43). The latter processes are obtained from one another by the exchange of an electron, such that their interference terms contribute with a negative sign.

5. Hole current process, exchange contribution

The last remaining diagram constitutes the exchange contribution of the hole current process of Sec. VI B 3. The diagram is displayed in Fig. 12 and generates the Keldysh space expression (C11), which subsequently simplifies to

$$I_R^{2c} = \frac{e}{2\pi}\frac{\Gamma^2}{4}\int_{\mu_I-\omega_R}^{\omega_L-\mu_I} d\omega''\,\Xi^*(\omega'')\Xi(\omega_L-\omega_R-\omega'') \times [\theta(\mu_R-\omega_R)-\theta(2\mu_I-\mu_L-\omega_R)] \times [\theta(\mu_L-\omega_L)-\theta(2\mu_I-\omega_R-\omega_L)], \quad (48)$$

contributing with the opposite sign of (45).

For contact interaction, $\nu_q \equiv$ const, we find $\Xi \equiv \Upsilon$, such that all diagrams cancel. This reflects that two electrons cannot occupy the same position in the reservoir channel, such that no relaxation by means of contact interaction is possible. Intrachannel relaxation thus requires finite-range interactions between the charge carriers.

VII. INTERACTIONS BETWEEN RESERVOIR REGION AND SOURCE LEAD

Taking into account tunneling and interactions between several chiral channels, a consistent treatment requires to artificially close the system into a single edge with fixed chirality [28]. Upon inspection of the micrograph of the experimental sample shown in Fig. 1(a), one finds that the one-dimensional channels of the source and reservoir regions partly copropagate and partly counterpropagate. In a simplified model, we treat the source and reservoir components of the sample as parallel channels with the same chirality (see Fig. 13). To achieve the most basic consistent treatment, the

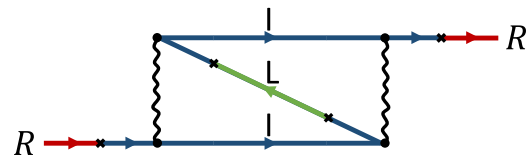

FIG. 12. Exchange diagram corresponding to the hole current process depicted in Fig. 6(c). The diagram reduces the current as a consequence of the indistinguishability of electrons.

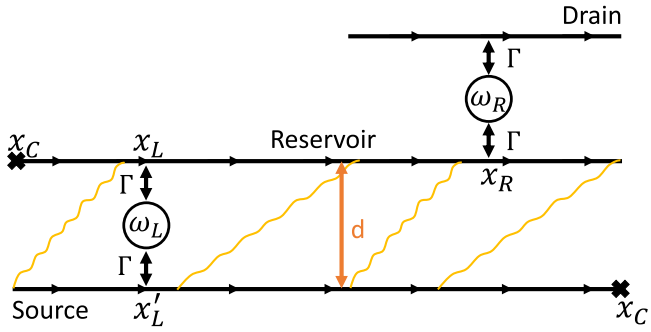

FIG. 13. Simple model for interchannel interaction between reservoir and source. To close the channels into a single edge with given chirality, a point x_C downstream of the emitter at x_L' in the source channel is identified with a point upstream of the emitter at x_L in the reservoir channel. The interaction is subsequently defined to be maximal when the distance of electrons in the reservoir channel measured from x_L coincides with the distance of electrons in the source channel measured from x_L'.

channels are connected by identifying a point in the source channel downstream of the emitter quantum dot with a point in the reservoir channel upstream of the emitter, denoted by x_C. Interaction of the charge carriers on the channels is further required to be maximal when their horizontal coordinates in Fig. 13 coincide, where coordinates in the reservoir and source channels are measured from the dot coordinates x_L and x_L', respectively.

Following these considerations, the interchannel interaction Hamiltonian takes the form[12]

$$H_V^{IL} = \frac{1}{2}\int_{x_C}^{\infty} dx_{\mathrm{Res}} \int_{-\infty}^{x_C} dx_{\mathrm{S}}\, v^d(x_{\mathrm{Res}} - x_L - x_{\mathrm{S}} + x_L') \times \hat{\psi}^{\dagger}_{x_{\mathrm{Res}}} \hat{\psi}^{\dagger}_{x_{\mathrm{S}}} \hat{\psi}_{x_{\mathrm{S}}} \hat{\psi}_{x_{\mathrm{Res}}} \tag{49}$$

as expressed in terms of spatial coordinates. The superscript of the interaction matrix element in position space v^d indicates accounting for the additional vertical channel separation d in Fig. 13. Taking x_C to infinity in the source channel and to negative infinity in the reservoir channel, reflecting that the point in which the channels close is located far away from the emitter quantum dot, the interaction Hamiltonian turns into

$$H_V^{IL} = \frac{1}{2\Omega}\sum_{k,k_L,q} v_q^d e^{iq(x_L - x_L')} \hat{r}^{\dagger}_{k-q} \hat{l}^{\dagger}_{k_L+q} \hat{l}_{k_L} \hat{r}_k. \tag{50}$$

The development of the Dyson equation for interchannel interaction (50) and the assignment of the respective Green's function components in Keldysh space proceeds similarly as in Sec. V. In contrast to that section, interchannel interactions no longer allow for the same concise representation of all possible processes as is provided by the truncated Dyson equation (25). Instead, the diagrams of all of these possible tunneling processes have to be considered at the second order of interactions, to be developed in Keldysh space. Afterward,

[12]Interactions between the reservoir region and the drain channel are not taken into account since at equal chemical potentials $\mu_I = \mu_R$ and $T = 0$, no inelastic processes are generated.

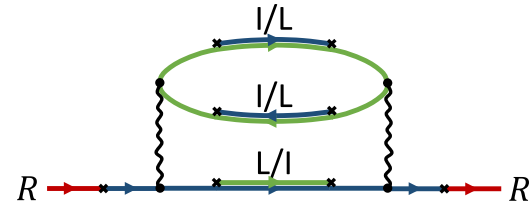

FIG. 14. Polarization contribution generated by interactions between charge carriers in the source lead and the reservoir region, showing relevant tunneling processes only.

similar approximations as in the case of intrachannel interactions are invoked.

In the diagrams generated by (50), the phase proportional to $x_L - x_L'$ shifts the tunneling coordinate x_L' in the source channel to the coordinate x_L in the reservoir channel, such that all currents become functions of the distance $\Delta x = x_R - x_L$, as it is the case for intrachannel interaction (27) [compare (39) and (44)].

The interaction (50) generates the second-order diagram shown in Fig. 14, in which only relevant tunneling processes are displayed. Polarization and exchange diagrams featuring both interchannel and intrachannel interaction are energetically strongly suppressed.

In the polarization diagram, the Green's function lines in the closed fermion loop here correspond to tunneling Green's functions of the source lead, which develop with the bare Hamiltonian H_0 as well as with the tunneling Hamiltonian H_T.

A. Corrections to elastic current

The interaction between source and reservoir channel (50) contributes a further polarization-diagram term to the interacting self-energy (30) [compare (31)] and thus to the corrected elastic current (33). This term is given by

$$E^2_{\mathrm{pol,IL}}(\omega) = \frac{1}{(2\pi v)^2}\int_0^{\mu_I-\omega} d\omega'\, \omega' \left(v^d_{\omega'/v}\right)^2. \tag{51}$$

Apart from the additional distance across the source quantum dot accounted for by v_q^d, the structure of (31) and (51) is identical. The latter term thus adds to the decay of the inelastic peak as the distance between the dots or the distance of the quantum dots' resonant levels from the Fermi level is increased. Exchange diagrams do not contribute for the relevant tunneling processes.[13]

[13]The interaction (50) also introduces a correction of the local (i.e., independent of tunneling phases) transition amplitude $\mathbf{t}_{\mathrm{D_L L}}\mathbf{g}^{V<}_{\mathrm{LL}}\mathbf{t}_{\mathrm{L D_L}} \simeq \mathbf{t}_{\mathrm{D_L L}}[\mathbf{g}^{<}_{\mathrm{LL}} + \mathbf{g}^{<}_{\mathrm{LL}}\mathbf{\Sigma}^{Va}_{\mathrm{LVL}}\mathbf{g}^{a}_{\mathrm{LL}} + \mathbf{g}^{r}_{\mathrm{LL}}\mathbf{\Sigma}^{V<}_{\mathrm{LVL}}\mathbf{g}^{a}_{\mathrm{LL}} + \mathbf{g}^{r}_{\mathrm{LL}}\mathbf{\Sigma}^{Vr}_{\mathrm{LVL}}\mathbf{g}^{<}_{\mathrm{LL}}]\mathbf{t}_{\mathrm{L D_L}}$ within the source lead, in which $\mathbf{g}^{V}_{\mathrm{LL}}$ denotes the Green's function including interactions but not tunneling. In the perturbative approach, the last three terms of the above amplitude diverge. Since the transition amplitude is local, a full solution only changes occupation probability and density of states in the left lead, without immediate influence on transfer processes and relaxation between the quantum dots. Such local corrections are therefore neglected.

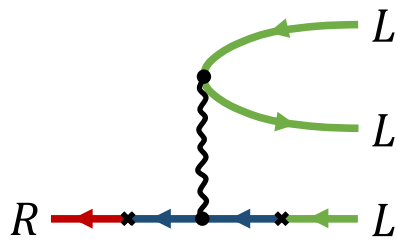

FIG. 15. Diagram describing the process in which the source electron, after tunneling into the reservoir region, creates an electron-hole pair in the source lead, before entering the detector quantum dot. The diagram is structurally equivalent to the diagram in Fig. 7, and reflects that the source lead provides a further decay channel when interactions between source and reservoir are taken into account.

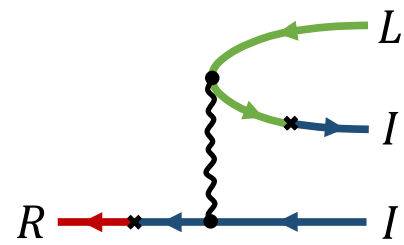

FIG. 16. (See also Ref. [16]) Diagram corresponding to the process in Fig. 17(a), in which the source electron interacts with the reservoir region where an electron-hole pair is created. The electron of the pair subsequently passes through the detector. The diagram creates current in triangle III in the experimental data shown in Fig. 1(b).

B. Inelastic contributions

Contributions to the inelastic current due to the interaction between source and reservoir channel (50) are described by the polarization diagram in Fig. 14. To evaluate the diagram, the tunneling Green's functions of the source lead which appear in the closed fermion loop have to be expanded on the Keldysh contour. This expansion is carried out in Appendix D. Here, equilibration in the self-energy Green's function lines for the relevant tunneling processes is restricted to the source and reservoir regions, as indicated in Fig. 14 [compare Fig. 4(a)].

After collection of terms which combine to the transition probability (19) through the left and right quantum dots, the contributions generated by the interaction (50) are identical in structure to the polarization diagram processes of Secs. VI B 1, VI B 2, and VI B 3, respectively, with the exception of two properties: the additional distance d across the emitter quantum dot (see Fig. 13) is accounted for by the replacement of the momentum-space interaction matrix element ν_q by ν_q^d, and tunneling through the emitter quantum dot on the fermion loop Green's function lines in Fig. 14 here fixes the energy of the tunneling electron in the reservoir region instead of in the source lead. In the following, we find that the latter distinction leads to the generation of triangles III and IV observed in the experimental data displayed in Fig. 1(b).

1. Direct electron current process

Taking into account interactions between reservoir and source (50), the first diagram under consideration is shown in Fig. 15. The expression generated by the diagram is identical to the contribution of the diagram in Fig. 7, with the exception of the modification due to the additional distance across the emitter quantum dot. The present diagram therefore contributes

$$\begin{aligned} I_R^{3a} = \frac{e}{2\pi}\frac{\Gamma^2}{4}&(\omega_L-\omega_R)|\Upsilon_d(\omega_L-\omega_R)|^2 \\ &\times[\theta(\mu_R-\omega_R)-\theta(\mu_L-\omega_R)] \\ &\times[\theta(\omega_R-\omega_L)-\theta(\mu_L-\omega_L)], \end{aligned} \tag{52}$$

where

$$\Upsilon_d(\omega'') = \frac{\nu^d_{\omega''/v}}{v}\frac{\Delta x}{v} \tag{53}$$

[compare (39) and (42)]. The diagram in Fig. 15 thus adds a further term to the current generated in triangle I in Fig. 1(b) since the interaction with the source lead provides an additional decay channel for reservoir electrons.

2. Inverted triangle electron swap

The second diagram generated by (50) is shown in Fig. 16. The physical process corresponding to the diagram is displayed in Fig. 17(a). Here, a virtual photon from the source generates an electron-hole pair in the reservoir region. The electron of the pair subsequently enters the drain channel via the detector quantum dot. The diagram is structurally equivalent to the diagram in Fig. 10 and contributes

$$\begin{aligned} I_R^{3b} = -\frac{e}{(2\pi)^3}&\int_{-\infty}^{\infty}d\omega''\int_{-\infty}^{\infty}d\omega'\int_{-\infty}^{\infty}d\omega\mathcal{T}_L(\omega'+\omega'')\mathcal{T}_R(\omega) \\ &\times[f_R(\omega)[f_I(\omega+\omega'')-1]f_I(\omega'+\omega'')[f_L(\omega')-1] \\ &-\text{“}f\leftrightarrow(f-1)\text{”}]|\Xi_d(\omega'')|^2, \end{aligned} \tag{54}$$

where the emitter quantum dot transition here fixes the energy $\omega'+\omega''$ in the reservoir region. At zero temperature, for δ-like filters (37), and $\mu_I=\mu_R$, we find

$$\begin{aligned} I_R^{3b} = \frac{e}{2\pi}\frac{\Gamma^2}{4}&\int_{\omega_L-\mu_L}^{\mu_I-\omega_R}d\omega''\,|\Xi_d(\omega'')|^2 \\ &\times[\theta(\mu_R-\omega_R)-\theta(\mu_L-\omega_R)] \\ &\times[\theta(\mu_I-\omega_L)-\theta(\mu_L+\mu_I-\omega_L-\omega_R)], \end{aligned} \tag{55}$$

where

$$\Xi_d(\omega'') = -\frac{1}{2\pi}\int_{-\infty}^{\infty}dq\,\nu_q^d\frac{\exp\left(i\frac{\Delta x}{v}(vq-\omega'')\right)}{(vq-\omega''-i\delta)^2}. \tag{56}$$

The second and third lines of (55) describe the outline of triangle III in Fig. 1(b). For $d=0$, (55) constitutes the mirror image of (43) with respect to the ω_L coordinate, reflected at $(\mu_I+\mu_L)/2$.

3. Inverted triangle hole current

The third and final diagram generated by (50) is depicted in Fig. 18, and the corresponding physical process is shown in

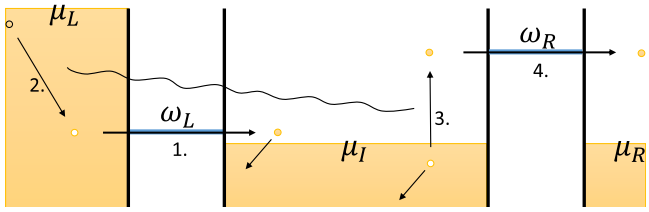

(a) Inverted triangle electron swap process

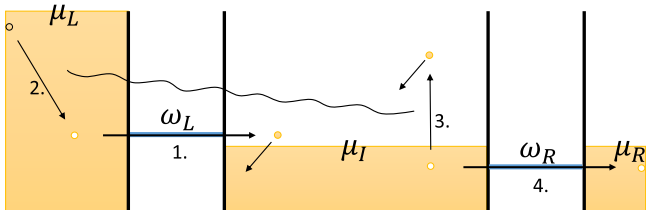

(b) Inverted triangle hole current process

FIG. 17. Introducing interactions between reservoir and source channels of the sample, three further inelastic second-order processes generate inelastic current: the first process (not shown) is equivalent to the process displayed in Fig. 6(a), with the exception that the electron-hole pair is generated in the source lead. (a) In the second process, (1.) an electron of the source lead enters the reservoir region. This electron is (2.) subsequently replaced by a further source electron dissipating energy. This energy (3.) creates an electron-hole pair in the reservoir region. The electron of the pair then (4.) enters the drain lead, where the absolute distance of the detector quantum dot energy from the Fermi level can be larger than the corresponding distance for the emitter. This process generates the upper left triangle in Fig. 1(b). (b) In the third process, the hole of the pair enters the drain when the detector energy is located below the Fermi level.

Fig. 17(b). Here, the hole of the electron-hole pair generated by the virtual photon from the source enters the detector quantum dot. The contribution of the diagram is given by

$$I_R^{3c} = -\frac{e}{2\pi}\frac{\Gamma^2}{4}\int_{\mu_R-\omega_R}^{\mu_L-\omega_L} d\omega'' \,|\Xi_d(\omega'')|^2 \times [\theta(\mu_L-\omega_L)-\theta(\mu_R-\omega_L)] \times [\theta(\mu_R-\omega_R)-\theta(\mu_R-\mu_L+\omega_L-\omega_R)]. \quad (57)$$

The second and third lines of (57) describe the outline of triangle IV observed in the measurement data of Fig. 1(b). Also in this case, for $d = 0$ the contribution is the exact

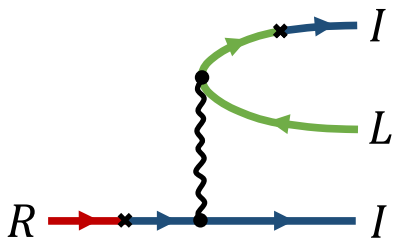

FIG. 18. Diagram corresponding to the process of Fig. 17(b). In this process, the hole of an electron-hole pair, created in the reservoir by a virtual photon from the source, enters the detector. The diagram generates current in triangle IV in Fig. 1(b).

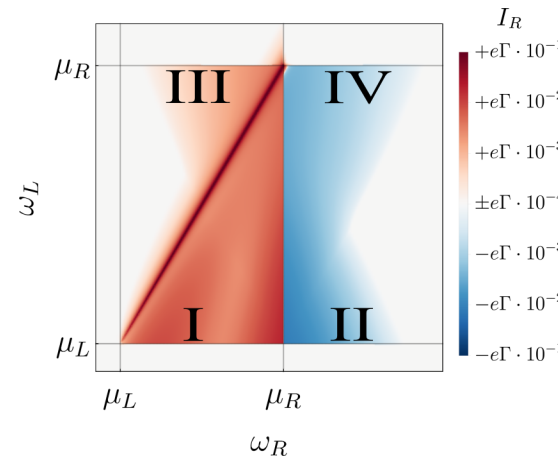

FIG. 19. (See also Ref. [16]) Drain current I_R on logarithmic scale. The processes depicted in Figs. 6(a), 6(b), and 6(c), caused by interactions in the reservoir region, generate current in the lower red and blue triangles [compare triangles I and II in Fig. 1(b)]. The processes of Figs. 17(a) and 17(b), due to interactions between the reservoir region and the source lead, generate current in the inverted red and blue triangles [compare triangles III and IV in Fig. 1(b)]. The present approach does not account for strong enough interactions to completely suppress the elastic current, as seen in the experimental data. (Parameters are $\mu_L = \mu_R + 400\Gamma$, $v = 260\lambda\Gamma$, $v_0 = 720\lambda\Gamma$, $\Delta x = 8\lambda$, $d = 2.8\lambda$.)

mirror image of the regular hole current (45), with respect to reflection of ω_L at $(\mu_I + \mu_L)/2$.

VIII. DRAIN CURRENT FOR FINITE-RANGE MODEL INTERACTION

In this section, all contributions resulting from interaction Hamiltonians (27) and (50) are evaluated explicitly for the model interaction (35), previously employed in Sec. VI A. In the source-reservoir interaction (50) the additional distance across the emitter quantum dot is phenomenologically accounted for by the factor[14]

$$v_q^d = v_q \exp\left(-\frac{d}{\lambda}\right), \quad (58)$$

in which d corresponds to the spatial separation of source and reservoir channels. To obtain the current, the function Ξ, defined in (44), has to be evaluated. Subsequently the energy integrals in (43), in (47), and in (48) have to be carried out to determine all inelastic contributions to the current. Evaluation and results for these integrals are presented in Appendix E.

In Fig. 19, the total drain current, accounting for all elastic and inelastic contributions presented in Secs. IV, VI, and VII, is displayed on a logarithmic scale that preserves the current's sign. As anticipated in these sections, current is generated in all distinct regions in the space of detector and emitter energy in which the experiment shows a clear signal [compare Fig. 1(b)]. The contributions to the current in the individual triangles I–IV in Figs. 1(b) and 19 are listed in Table I.

[14]The Fourier transform (28) of (35) is proportional to $\exp(-r/\lambda)$.

TABLE I. List of contributions in triangles I–IV to drain current in Figs. 1(b) and 19 due to inelastic processes.

Triangle	Contribution (Eq. No.)
I	I_R^{1a} (42), I_R^{1b} (43), I_R^{2a} (46), I_R^{2b} (47), I_R^{3a} (52)
II	I_R^{1c} (45), I_R^{2c} (48)
III	I_R^{3b} (55)
IV	I_R^{3c} (57)

While the reduction of the hole current (to the extent that the signal changes sign) along the hypotenuse of triangle II in the measurement data displayed in Fig. 1(b) at $\omega_L - \mu_R \simeq \mu_R - \omega_R$ is mainly due to an excited state of the detector dot [15], the reduction in Fig. 19 at similar energies stems from the exchange diagram in Fig. 12, reducing the current as a consequence of the indistinguishability of electrons. Higher-order interaction terms in a model with several channels per edge, accounting for processes in which a reservoir electron excites an electron-hole pair in another channel, which in turn excites an electron-hole pair back in the reservoir, are not subject to such a suppression since the exchange diagram does not appear for interchannel interactions at the relevant tunneling order.

In the experimental data, the elastic peak is not visible anymore already for comparably small dot energies. While the perturbative calculation to second order in interactions indicates a diminishing elastic signal, the absence of the elastic line for higher filter energies escapes the approximation's admissible interaction strength.

Figure 20 shows the drain current along a line cut in ω_R at constant ω_L, for increasing dot separation Δx. With the separation also the transfer time $\Delta x/v$ increases, such that the sequence in Fig. 20 can be viewed as the temporal evolution of the electronic system in the channel (cf. Ref. [18]). With the decrease of the elastic contribution, inelastic contributions intensify. While the process of Fig. 6(a) leads to a current displaying a maximum next to the elastic peak at $\omega_L = \omega_R$, all remaining inelastic processes contribute close to and above [processes in Figs. 6(b) and 17(a)] or below [processes in Figs. 6(c) and 17(b)] the Fermi level. The reason for this localization in energy space is that a screened interaction, such as (35), is suppressed with increasing energy of virtual photons. While the photon energy (measured in units of v/λ) for the former process is determined by the energy difference of the filters $\omega_L - \omega_R$, for the latter processes this energy depends on the distance of the filter energies from the Fermi level $\omega_R - \mu_R$ and $\omega_L - \mu_R$, respectively.

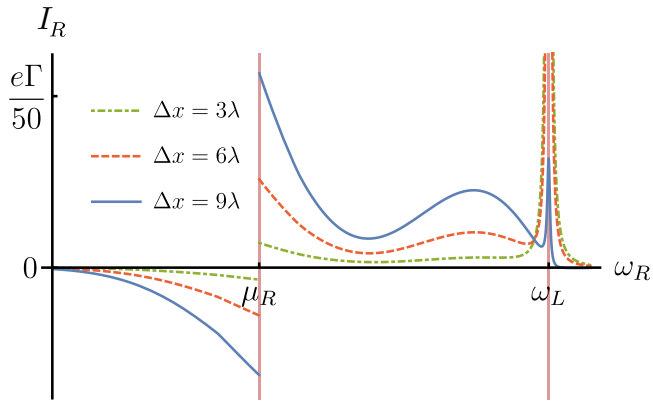

FIG. 20. Detector current I_R for increasing spatial separation Δx between emitter and detector quantum dots. As the elastic peak at $\omega_L = \omega_R$ diminishes for increasing separation, inelastic contributions intensify. The curve for the value $x = 9\lambda$ (full line) is close to the boundary of validity of the approach [cf. (34)], after which the elastic current takes on negative values and the approximation becomes unphysical. While the peak next to the elastic contribution is associated with processes in which the initial electron is directly transferred [see Fig. 6(a)], the peaks close to the Fermi energy μ_R are associated with processes in which a charge carrier from the Fermi sea enters the detector, both for the regular triangles in Figs. 6(b) and 6(c), as well as for the inverted triangles, Figs. 17(a) and 17(b). (Parameters are $\mu_L = \mu_R + 400\Gamma$, $\omega_L = \mu_R + 350\Gamma$, $v = 260\lambda\Gamma$, $\nu_0 = 720\lambda\Gamma$, $d = 2.8\lambda$.)

IX. SUMMARY AND OUTLOOK

A perturbative diagrammatic approach allows to relate individual signals measured in the ETH electron spectrometer to underlying physical processes. As a central point, the analysis shows that interactions between electrons in source and reservoir of the experimental sample generate current in regions of the detector-emitter energy landscape, in which the detector energy can exceed the emitter energy, thus giving rise to triangles III and IV in the measurement data displayed in Fig. 1(b). These currents are generated by Auger-type recombination processes in which the recombination energy is directly transferred from the source channel to the reservoir region. Thereby charge carriers are generated in the reservoir region at energies that can exceed the energy of electrons emitted from the source.

The experimental detection of energy transfer between leads and the central edge of the electron spectrometer, in combination with our theoretical analysis, suggests that such processes might have a significant impact on relaxation characteristics of mesoscopic devices, and that this decay channel cannot in general be readily neglected, as has previously been conjectured [12]. It would be interesting to see in a quantitative study whether Auger-type processes can account for a significant amount of the energy loss reported in Refs. [10,14]. Charge transfer based on capacitive coupling has previously been reported also in different systems in Refs. [29,30].

For finite-range interactions, our approach furthermore demonstrates that processes, in which the original source electron enters the detector after dissipating some of its energy, contribute close to the elastic line, i.e., at comparable dot energies. Processes in which the original electron is exchanged for a charge carrier from the Fermi sea contribute close to the Fermi level.

The perturbative nature of the approach in interactions limits its validity in terms of maximally admissible quantum dot energies (as measured from the Fermi energy), interaction strength, screening length, and spatial separation of quantum dots (see discussion in the last paragraph of Sec. VI A), as well as number of interaction events. As a consequence, the present treatment is not suitable to quantitatively reproduce the signal measured in the sample, and to account for the absence of the

elastic line in the measurement data at higher quantum dot energies. Relaxation due to interchannel interaction between several channels in the reservoir edge cannot fully be captured by second-order perturbation theory. Since this relaxation mechanism is not inhibited by Pauli blocking, it likely constitutes the dominant relaxation channel generating inelastic currents in triangles I and II. To extend the applicability of the formalism to the aforementioned scenarios, it is necessary to include higher-order interaction terms.

At filling factor $\nu = 2$, it has been shown in principle [31], and recently been realized on a large scale in an interferometer setup [32], that the inner edge channel can be rendered energetically inaccessible for excitations from the outer edge channel. This is achieved by closing the inner channel into short loops such that the quantized excitation energy of these loops exceeds the available energy in the current-carrying outer edge channel. In such a system, relaxation should predominantly be caused by interactions within the same channel.

A full-scale nonequilibrium bosonization approach [23,33–38] describing interactions exactly, including also effects of interchannel interaction within the reservoir region, poses a particular challenge when tunneling through the dots and finite-range interactions are accounted for simultaneously. Our perturbative treatment indicates which elements have to enter an attempt for a full bosonization solution that captures currents in triangles III and IV.

A further evident opportunity to apply the perturbative approach is the case in which the sample is not subject to an external magnetic field, such that electrons in the sample propagate in two dimensions. Here, the elastic line remains visible in the measurement data [15], indicating that this case lies well within the validity of second-order perturbation theory also at higher injection energies. Without the magnetic field, the geometry of the spectrometer plays a crucial role, with a significant enhancement of the signal at resonance energies of the sample. Within the general scheme of the present approach, such effects of geometry can be accommodated in the Green's functions that determine the transition amplitudes of the reservoir region.

ACKNOWLEDGMENTS

The authors would like to thank I. Gornyi, D. Polyakov and B. Rosenow, K. Ensslin, T. Ihn, M. Röösli, and T. Krähenmann, as well as A. Marguerite, K. Snizhko, and T. Holder, for useful discussions. Y.G. acknowledges funding from DFG Grant No. RO 2247/11-1, CRC 183 (Project C01), and the Italia-Israel project QUANTRA. Y.M. acknowledges support from ISF Grant No. 292/15. J.P. acknowledges support by the Koshland Foundation. S.G.F. is a BGU PD fellow and acknowledges financial support from the Minerva and Kreitman foundations.

APPENDIX A: DERIVATION OF GENERAL DRAIN CURRENT FORMULA

In this Appendix, the intermediate steps which lead to the general expression (8) for the drain current are presented. Following [24], the fact that the drain channel is assumed to be noninteracting allows us to expand

$$\mathbf{G}_{\mathrm{L_R D_R}} = \mathbf{g}_{\mathrm{L_R L_R}} \mathbf{t}_{\mathrm{L_R D_R}} \mathbf{G}_{\mathrm{D_R D_R}} \tag{A1}$$

in (7). Here, $\mathbf{g}_{\mathrm{L_R L_R}}$ denotes the Green's function of the drain lead which develops solely with the bare Hamiltonian H_0, and $\mathbf{G}_{\mathrm{D_R D_R}}$ denotes the Green's function of the detector quantum dot developing with the full Hamiltonian H. Expanding the Green's functions in (7) in their form (A1) on the Keldysh contour leads to the expression [24,27]

$$I_R = -\frac{e}{2\pi} \int_{-\infty}^{\infty} d\omega \, \mathrm{tr}\left\{ \mathbf{\Sigma}^{<}_{\mathrm{D_R L_R D_R}} \mathbf{G}^{>}_{\mathrm{D_R D_R}} - \mathbf{\Sigma}^{>}_{\mathrm{D_R L_R D_R}} \mathbf{G}^{<}_{\mathrm{D_R D_R}} \right\}. \tag{A2}$$

The Green's function of the detector quantum dot develops according to

$$\mathbf{G}_{\mathrm{D_R D_R}} = \bar{\mathbf{g}}_{\mathrm{D_R D_R}} + \bar{\mathbf{g}}_{\mathrm{D_R D_R}} \mathbf{\Sigma}_{\mathrm{D_R I D_R}} \bar{\mathbf{g}}_{\mathrm{D_R D_R}}. \tag{A3}$$

Expanding the lesser and greater Green's functions of the drain lead in (A2) in terms of (A3), on the Keldysh contour, according to the Langreth rules [27], we have for the lesser component

$$\begin{aligned} \mathbf{G}^{<}_{\mathrm{D_R D_R}} = {} & \bar{\mathbf{g}}^{<}_{\mathrm{D_R D_R}} + \bar{\mathbf{g}}^{<}_{\mathrm{D_R D_R}} \mathbf{\Sigma}^{a}_{\mathrm{D_R I D_R}} \bar{\mathbf{g}}^{a}_{\mathrm{D_R D_R}} \\ & + \bar{\mathbf{g}}^{r}_{\mathrm{D_R D_R}} \mathbf{\Sigma}^{<}_{\mathrm{D_R I D_R}} \bar{\mathbf{g}}^{a}_{\mathrm{D_R D_R}} + \bar{\mathbf{g}}^{r}_{\mathrm{D_R D_R}} \mathbf{\Sigma}^{r}_{\mathrm{D_R I D_R}} \bar{\mathbf{g}}^{<}_{\mathrm{D_R D_R}}. \end{aligned} \tag{A4}$$

The same relation follows for the greater component with "$<\to>$." After expansion of the lesser component of the Green's function (9) by means of the respective kinetic equation [27,39]

$$\bar{\mathbf{g}}^{<}_{\mathrm{D_R D_R}} = \bar{\mathbf{g}}^{r}_{\mathrm{D_R D_R}} \mathbf{\Sigma}^{<}_{\mathrm{D_R L_R D_R}} \bar{\mathbf{g}}^{a}_{\mathrm{D_R D_R}}, \tag{A5}$$

followed by subsequent insertion of (A5) into (A4), only the third term of (A4) (and of the latter's counterpart for the greater Green's function) contributes in (A2). To see this, the explicit expressions for the lesser and greater components of the drain lead's tunneling self-energy,

$$\begin{aligned} \mathbf{\Sigma}^{<}_{\mathrm{D_R L_R D_R}} &= \sum_{k_R} t^{*}_{k_R R} g^{<}_{k_R}(\omega) t_{k_R R} \\ &\to \int_{-\infty}^{\infty} dk_R \rho(\omega_{k_R}) t^{*}_{k_R R} g^{<}_{k_R}(\omega) t_{k_R R} \\ &= i\Gamma(\omega) f_R(\omega) \end{aligned} \tag{A6}$$

and

$$\mathbf{\Sigma}^{>}_{\mathrm{D_R L_R D_R}} = i\Gamma(\omega)(f_R(\omega) - 1), \tag{A7}$$

respectively, have to be inserted into (A2) and (A5). Thereby, the first, second, and fourth terms of (A4) cancel with the greater component counterpart in (A2) since the Fermi distributions of these terms are evaluated at the same chemical potential μ_R of the drain lead. Insertion of the remaining third term of (A4) into (A2) then leads to the desired general expression for the current (8).

Using the kinetic equations for the retarded and advanced components of the dot-lead Green's functions

$$\bar{\mathbf{g}}^{r/a}_{\mathrm{D_R D_R}} = \mathbf{g}^{r/a}_{\mathrm{D_R D_R}} + \mathbf{g}^{r/a}_{\mathrm{D_R D_R}} \mathbf{\Sigma}^{r/a}_{\mathrm{D_R L_R D_R}} \bar{\mathbf{g}}^{r/a}_{\mathrm{D_R D_R}}, \tag{A8}$$

and insertion of the explicit expressions for the lead self-energies in the wide-band approximation [24,27]

$$\mathbf{\Sigma}^{r/a}_{\mathrm{D_R L_R D_R}} \to \mp \frac{i}{2} \Gamma(\omega), \tag{A9}$$

allows to cast the general formula (8) for the current into the explicit form (12).

APPENDIX B: DERIVATION OF DRAIN CURRENT IN ABSENCE OF INTERACTIONS

In this Appendix, evaluation of expressions which determine the current (18) in the absence of interactions are presented. Upon insertion of (17) into (8), determination of the drain current requires evaluation of the following transition self-energies: the transition self-energy from the right dot to the left dot vanishes,

$$\mathbf{t}_{\mathrm{D_L I}}\mathbf{G}^{Tr}_{\mathrm{II}}\mathbf{t}_{\mathrm{ID_R}} = 0, \tag{B1}$$

since the channel is chiral with right-moving particles only. For the transition from left to right, we find the Dyson equation

$$\begin{aligned}\mathbf{t}_{\mathrm{D_R I}}\mathbf{G}^{Tr}_{\mathrm{II}}\mathbf{t}_{\mathrm{ID_L}} &= \mathbf{t}_{\mathrm{D_R I}}\mathbf{g}^{r}_{\mathrm{II}}\mathbf{t}_{\mathrm{ID_L}} + \mathbf{t}_{\mathrm{D_R I}}\mathbf{g}^{r}_{\mathrm{II}}\boldsymbol{\Sigma}^{r}_{\mathrm{ID_R I}}\mathbf{G}^{Tr}_{\mathrm{II}}\mathbf{t}_{\mathrm{ID_L}} \\ &\quad + \mathbf{t}_{\mathrm{D_R I}}\mathbf{g}^{r}_{\mathrm{II}}\boldsymbol{\Sigma}^{r}_{\mathrm{ID_L I}}\bar{\mathbf{g}}^{r}_{\mathrm{II}}\mathbf{t}_{\mathrm{ID_L}},\end{aligned} \tag{B2}$$

where

$$\boldsymbol{\Sigma}_{\mathrm{ID_{L/R}I}} = \mathbf{t}_{\mathrm{ID_{L/R}}}\bar{\mathbf{g}}_{\mathrm{D_{L/R}D_{L/R}}}\mathbf{t}_{\mathrm{D_{L/R}I}}, \tag{B3}$$

with

$$\bar{\mathbf{g}}_{\mathrm{II}} = \mathbf{g}_{\mathrm{II}} + \mathbf{g}_{\mathrm{II}}\boldsymbol{\Sigma}_{\mathrm{ID_L I}}\bar{\mathbf{g}}_{\mathrm{II}}. \tag{B4}$$

The Dyson equation (B2) reflects that charge carriers can only pass from the left dot to the right dot once, before and after tunneling back and forth between the reservoir and each of the dots. For the local self-energy at the left dot, we find

$$\mathbf{t}_{\mathrm{D_L I}}\mathbf{G}^{Tr}_{\mathrm{II}}\mathbf{t}_{\mathrm{ID_L}} = \mathbf{t}_{\mathrm{D_L I}}\bar{\mathbf{g}}^{r}_{\mathrm{II}}\mathbf{t}_{\mathrm{ID_L}}. \tag{B5}$$

An analogous equation holds for the local self-energy at the right dot since going back and forth between the left and the right dots is prohibited in the chiral channel. The corresponding relations for the advanced Green's functions are obtained by complex conjugation.

The final building blocks to obtain an explicit expression for the current are the transition self-energies for the bare Green's functions of the intermediate region, which are given by

$$\begin{aligned}\mathbf{t}_{\mathrm{D_L I}}\mathbf{g}^{r}_{\mathrm{II}}\mathbf{t}_{\mathrm{ID_R}} &= 0, \\ \mathbf{t}_{\mathrm{D_R I}}\mathbf{g}^{r}_{\mathrm{II}}\mathbf{t}_{\mathrm{ID_L}} &= -i\Gamma e^{+i\frac{\Delta x}{v}\omega}, \\ \mathbf{t}_{\mathrm{D_L I}}\mathbf{g}^{r}_{\mathrm{II}}\mathbf{t}_{\mathrm{ID_L}} &= -\frac{i\Gamma}{2}, \\ \mathbf{t}_{\mathrm{D_R I}}\mathbf{g}^{r}_{\mathrm{II}}\mathbf{t}_{\mathrm{ID_R}} &= -\frac{i\Gamma}{2},\end{aligned} \tag{B6}$$

where also here the advanced components are obtained by complex conjugation, as well as by

$$\begin{aligned}\mathbf{t}_{\mathrm{D_L I}}\mathbf{g}^{<}_{\mathrm{II}}\mathbf{t}_{\mathrm{ID_R}} &= i\Gamma f_I(\omega)e^{-i\frac{\Delta x}{v}\omega}, \\ \mathbf{t}_{\mathrm{D_R I}}\mathbf{g}^{<}_{\mathrm{II}}\mathbf{t}_{\mathrm{ID_L}} &= i\Gamma f_I(\omega)e^{+i\frac{\Delta x}{v}\omega}, \\ \mathbf{t}_{\mathrm{D_L I}}\mathbf{g}^{<}_{\mathrm{II}}\mathbf{t}_{\mathrm{ID_L}} &= i\Gamma f_I(\omega), \\ \mathbf{t}_{\mathrm{D_R I}}\mathbf{g}^{<}_{\mathrm{II}}\mathbf{t}_{\mathrm{ID_R}} &= i\Gamma f_I(\omega),\end{aligned} \tag{B7}$$

where $\Delta x = x_R - x_L > 0$. The respective greater Green's functions are obtained by the replacement "$f \to (f-1)$."

Solving the above Dyson equations (B2) and (B4), and insertion of the explicit transition self-energies (B6) and (B7) into (8), leads to the explicit current (18) of the noninteracting system.

APPENDIX C: CONTRIBUTIONS DUE TO RESERVOIR ELECTRON INTERACTIONS

In this Appendix, Green's function expressions which give rise to changes of the elastic current as well as to inelastic contributions due to reservoir electron interactions are collected.

1. Green's function expressions for corrections to elastic current

Insertion of the second and fourth terms of expansion (26) into the general expression for the current (8), and expansion of the lesser/greater Green's functions of the reservoir region (17), leads to

$$\begin{aligned}I_R^{\mathrm{corr}} = -\frac{e}{2\pi}\int_{-\infty}^{\infty} d\omega \Big[&\mathrm{tr}\Big\{\bar{\mathbf{g}}^{a}_{\mathrm{D_R D_R}}\boldsymbol{\Sigma}^{<}_{\mathrm{D_R L_R D_R}}\bar{\mathbf{g}}^{r}_{\mathrm{D_R D_R}}\mathbf{t}_{\mathrm{D_R I}}\mathbf{G}^{Tr}_{\mathrm{II}}\mathbf{t}_{\mathrm{ID_L}}\bar{\mathbf{g}}^{r}_{\mathrm{D_L D_L}}\boldsymbol{\Sigma}^{>}_{\mathrm{D_L L_L D_L}}\bar{\mathbf{g}}^{a}_{\mathrm{D_L D_L}}\mathbf{t}_{\mathrm{D_L I}}\mathbf{G}^{Ta}_{\mathrm{II}}\boldsymbol{\Sigma}^{a}_{\mathrm{IVI}}\mathbf{G}^{Ta}_{\mathrm{II}}\mathbf{t}_{\mathrm{ID_R}} \\ &+ \bar{\mathbf{g}}^{a}_{\mathrm{D_R D_R}}\boldsymbol{\Sigma}^{<}_{\mathrm{D_R L_R D_R}}\bar{\mathbf{g}}^{r}_{\mathrm{D_R D_R}}\mathbf{t}_{\mathrm{D_R I}}\mathbf{G}^{Tr}_{\mathrm{II}}\boldsymbol{\Sigma}^{r}_{\mathrm{IVI}}\mathbf{G}^{Tr}_{\mathrm{II}}\mathbf{t}_{\mathrm{ID_L}}\bar{\mathbf{g}}^{r}_{\mathrm{D_L D_L}}\boldsymbol{\Sigma}^{>}_{\mathrm{D_L L_L D_L}}\bar{\mathbf{g}}^{a}_{\mathrm{D_L D_L}}\mathbf{t}_{\mathrm{D_L I}}\mathbf{G}^{Ta}_{\mathrm{II}}\mathbf{t}_{\mathrm{ID_R}}\Big\} - \text{“}<\leftrightarrow>\text{”}\Big].\end{aligned} \tag{C1}$$

For the model interaction (35), we obtain for the polarization diagram term (31) the contribution

$$E^2_{\mathrm{pol}}(\omega) = \frac{1}{(2\pi)^2}\frac{\nu_0^2}{2\lambda^2}\frac{\frac{\lambda^2}{v^2}(\mu_I-\omega)^2}{1+\frac{\lambda^2}{v^2}(\mu_I-\omega)^2}, \tag{C2}$$

and for the exchange diagram term (32) the contribution

$$E^2_{\mathrm{exch}}(\omega) = \frac{1}{(2\pi)^2}\frac{\nu_0^2}{\lambda^2}\left[\arctan^2\left(\frac{\lambda}{v}(\mu_I-\omega)\right) - h\left(\frac{\lambda}{v}(\mu_I-\omega)\right)\right], \tag{C3}$$

in which

$$h(x) = x\int_0^1 dy\frac{\arctan(xy)}{1+x^2(1-y)^2}. \tag{C4}$$

The poles of (C2) are located at $\omega = \mu \pm iv/\lambda$ and $E^2_{\rm pol}(\omega \to \infty) \to v_0^2/2(2\pi\lambda)^2$ in the complex plane. A numerical comparison shows that (C3) has a similar pole structure as (C2) and $E^2_{\rm exch}(\omega \to \infty) \to 0$ in the complex plane.

In (C1), the poles of (C2) contribute terms that decay as $\exp(-\Delta x/\lambda)$. Due to the similarity of the pole structure of (C3), we expect a similar decay also in the exchange contribution. Neglecting the poles of (C2) and (C3), the corrected transition self-energies in (C1) are given by

$$\mathbf{t}_{\mathrm{D_R I}}\mathbf{G}^{Tr}_{\mathrm{II}}\boldsymbol{\Sigma}^{r}_{\mathrm{IVI}}\mathbf{G}^{Tr}_{\mathrm{II}}\mathbf{t}_{\mathrm{ID_L}} \simeq \mathbf{t}_{\mathrm{D_R I}}\mathbf{g}^{r}_{\mathrm{II}}\big[\mathbf{g}^{r}_{\mathrm{II}}E^2(vk)\big]\mathbf{g}^{r}_{\mathrm{II}}\mathbf{t}_{\mathrm{ID_L}} \simeq \frac{i\Gamma}{2}\frac{\partial^2}{\partial k^2}[\exp(i\Delta x k)E(vk)]\Big|_{k=\frac{\omega}{v}}. \tag{C5}$$

According to the above considerations, the approximation in the second line of (C5) is justified as long as $\lambda \ll \Delta x$. Combining all terms in (C1) then generates the second and third terms in (33). We neglect the third term, which is suppressed against the second term by a factor of $\lambda^2/\Delta x^2$.

For the evaluation of the ω integral in (33) we take into account residues of $\mathcal{T}_{L/R}$ and not of E^2. For (C2), the contribution of the latter is suppressed by a factor of $2(1/2\pi)^3(v_0/v)^2(\Delta x/\lambda)^2(\Gamma\lambda/v)^3$ against the maximum of the elastic current, given $\mu_L - \mu_R \sim v/\lambda$.

2. Inelastic contributions in terms of Green's functions

After collection of all tunneling terms which correspond to one electron or hole transmission per quantum dot, and discarding the remaining terms, no tunneling amplitudes remain in the reservoir equilibration term in (36),

$$\big(\mathbf{I} + \mathbf{G}^{Tr}_{\mathrm{II}}\boldsymbol{\Sigma}^{r}_{\mathrm{ITI}}\big)\mathbf{g}^{</>}_{\mathrm{II}}\big(\mathbf{I} + \boldsymbol{\Sigma}^{a}_{\mathrm{ITI}}\mathbf{G}^{Ta}_{\mathrm{II}}\big) \to \mathbf{g}^{</>}_{\mathrm{II}}. \tag{C6}$$

After the initial approximation (C6), the contributions due to the diagrams in Figs. 7, 9, 10, 11(a), and 12 are, respectively, given by

$$\begin{aligned} I_R^{\mathrm{1a}} = -\frac{e}{2\pi}\int_{-\infty}^{\infty} d\omega''\, \nu_{\mathrm{Q}}^2\Bigg[\frac{1}{2\pi\,\Omega}\int_{-\infty}^{\infty} d\omega'\,\mathrm{tr}\big\{\mathbf{g}^{<}_{\mathrm{I+QI+Q}}(\omega'+\omega'')\mathbf{g}^{>}_{\mathrm{II}}(\omega')\big\} \\ \times\frac{1}{2\pi\,\Omega}\int_{-\infty}^{\infty} d\omega\,\mathrm{tr}\big\{\bar{\mathbf{g}}^{a}_{\mathrm{D_R D_R}}(\omega)\boldsymbol{\Sigma}^{<}_{\mathrm{D_R L_R D_R}}(\omega)\bar{\mathbf{g}}^{r}_{\mathrm{D_R D_R}}(\omega)\mathbf{t}_{\mathrm{D_R I}}\mathbf{G}^{Tr}_{\mathrm{II}}(\omega)\mathbf{G}^{Tr}_{\mathrm{I+QI}}(\omega+\omega'')\mathbf{t}_{\mathrm{ID_L}} \\ \times\bar{\mathbf{g}}^{r}_{\mathrm{D_L D_L}}(\omega+\omega'')\boldsymbol{\Sigma}^{>}_{\mathrm{D_L L_L D_L}}(\omega+\omega'')\bar{\mathbf{g}}^{a}_{\mathrm{D_L D_L}}(\omega+\omega'')\mathbf{t}_{\mathrm{D_L I}}\mathbf{G}^{Ta}_{\mathrm{II+Q}}(\omega+\omega'')\mathbf{G}^{Ta}_{\mathrm{II}}(\omega)\mathbf{t}_{\mathrm{ID_R}}\big\} - \text{“}<\leftrightarrow>\text{”}\Bigg], \end{aligned} \tag{C7}$$

$$\begin{aligned} I_R^{\mathrm{1b}} = -\frac{e}{2\pi}\int_{-\infty}^{\infty} d\omega''\,\nu_Q\nu_{Q'}\Bigg[\frac{1}{2\pi\,\Omega}\int_{-\infty}^{\infty} d\omega'\,\mathrm{tr}\big\{\bar{\mathbf{g}}^{r}_{\mathrm{D_L D_L}}(\omega')\boldsymbol{\Sigma}^{>}_{\mathrm{D_L L_L D_L}}(\omega')\bar{\mathbf{g}}^{a}_{\mathrm{D_L D_L}}(\omega') \\ \times\mathbf{t}_{\mathrm{D_L I}}\mathbf{G}^{Ta}_{\mathrm{II+Q}}(\omega')\mathbf{g}^{<}_{\mathrm{I+Q+Q'I+Q+Q'}}(\omega'+\omega'')\mathbf{G}^{Tr}_{\mathrm{I+Q'I}}(\omega')\mathbf{t}_{\mathrm{ID_L}}\big\} \\ \times\frac{1}{2\pi\,\Omega}\int_{-\infty}^{\infty} d\omega\,\mathrm{tr}\big\{\bar{\mathbf{g}}^{a}_{\mathrm{D_R D_R}}(\omega)\boldsymbol{\Sigma}^{<}_{\mathrm{D_R L_R D_R}}(\omega)\bar{\mathbf{g}}^{r}_{\mathrm{D_R D_R}}(\omega) \\ \times\mathbf{t}_{\mathrm{D_R I}}\mathbf{G}^{Tr}_{\mathrm{II+Q'}}(\omega)\mathbf{g}^{>}_{\mathrm{I+Q+Q'I+Q+Q'}}(\omega+\omega'')\mathbf{G}^{Ta}_{\mathrm{I+QI}}(\omega)\mathbf{t}_{\mathrm{ID_R}}\big\} - \text{“}<\leftrightarrow>\text{”}\Bigg], \end{aligned} \tag{C8}$$

$$\begin{aligned} I_R^{\mathrm{1c}} = -\frac{e}{2\pi}\int_{-\infty}^{\infty} d\omega''\,\nu_Q\nu_{Q'}\Bigg[\frac{1}{2\pi\,\Omega}\int_{-\infty}^{\infty} d\omega'\,\mathrm{tr}\big\{\bar{\mathbf{g}}^{r}_{\mathrm{D_L D_L}}(\omega')\boldsymbol{\Sigma}^{<}_{\mathrm{D_L L_L D_L}}(\omega')\bar{\mathbf{g}}^{a}_{\mathrm{D_L D_L}}(\omega') \\ \times\mathbf{t}_{\mathrm{D_L I}}\mathbf{G}^{Ta}_{\mathrm{II+Q}}(\omega')\mathbf{g}^{>}_{\mathrm{II}}(\omega'+\omega'')\mathbf{G}^{Tr}_{\mathrm{I+Q'I}}(\omega')\mathbf{t}_{\mathrm{ID_L}}\big\} \\ \times\frac{1}{2\pi\,\Omega}\int_{-\infty}^{\infty} d\omega\,\mathrm{tr}\big\{\bar{\mathbf{g}}^{a}_{\mathrm{D_R D_R}}(\omega)\boldsymbol{\Sigma}^{<}_{\mathrm{D_R L_R D_R}}(\omega)\bar{\mathbf{g}}^{r}_{\mathrm{D_R D_R}}(\omega) \\ \times\mathbf{t}_{\mathrm{D_R I}}\mathbf{G}^{Tr}_{\mathrm{II+Q'}}(\omega)\mathbf{g}^{>}_{\mathrm{I+Q+Q'I+Q+Q'}}(\omega+\omega'')\mathbf{G}^{Ta}_{\mathrm{I+QI}}(\omega)\mathbf{t}_{\mathrm{ID_R}}\big\} - \text{“}<\leftrightarrow>\text{”}\Bigg], \end{aligned} \tag{C9}$$

$$\begin{aligned} I_R^{\mathrm{2a}} = \frac{e}{2\pi}\nu_Q\nu_{Q'}\int_{-\infty}^{\infty} d\omega''\int_{-\infty}^{\infty} d\omega'\int_{-\infty}^{\infty} d\omega\,\frac{1}{(2\pi\,\Omega)^2}\Bigg[\mathrm{tr}\big\{\bar{\mathbf{g}}^{a}_{\mathrm{D_R D_R}}(\omega)\boldsymbol{\Sigma}^{<}_{\mathrm{D_R L_R D_R}}(\omega)\bar{\mathbf{g}}^{r}_{\mathrm{D_R D_R}}(\omega) \\ \times\mathbf{t}_{\mathrm{D_R I}}\mathbf{G}^{Tr}_{\mathrm{II}}(\omega)\mathbf{G}^{Tr}_{\mathrm{I+QI}}(\omega+\omega'')\mathbf{t}_{\mathrm{ID_L}}\bar{\mathbf{g}}^{r}_{\mathrm{D_L D_L}}(\omega+\omega'')\boldsymbol{\Sigma}^{>}_{\mathrm{D_L L_L D_L}}(\omega+\omega'')\bar{\mathbf{g}}^{a}_{\mathrm{D_L D_L}}(\omega+\omega'') \\ \times\mathbf{t}_{\mathrm{D_L I}}\mathbf{G}^{Ta}_{\mathrm{II+Q}}(\omega+\omega'')\mathbf{g}^{<}_{\mathrm{I+Q+Q'I+Q+Q'}}(\omega+\omega'+\omega'')\mathbf{g}^{>}_{\mathrm{I+Q'I+Q'}}(\omega+\omega')\mathbf{G}^{Ta}_{\mathrm{II}}(\omega)\mathbf{t}_{\mathrm{ID_R}}\big\} - \text{“}<\leftrightarrow>\text{”}\Bigg], \end{aligned} \tag{C10}$$

$$I_R^{\mathrm{2c}} = \frac{e}{2\pi}\nu_Q\nu_{Q'}\int_{-\infty}^{\infty} d\omega''\int_{-\infty}^{\infty} d\omega'\int_{-\infty}^{\infty} d\omega$$

$$\times \frac{1}{(2\pi\Omega)^2}\Big[\mathrm{tr}\big\{\bar{\mathbf{g}}^a_{\mathrm{D_R D_R}}(\omega)\boldsymbol{\Sigma}^<_{\mathrm{D_R L_R D_R}}(\omega)\bar{\mathbf{g}}^r_{\mathrm{D_R D_R}}(\omega)\mathbf{t}_{\mathrm{D_R I}}\mathbf{G}^{Tr}_{\mathrm{II}}(\omega)\mathbf{g}^>_{\mathrm{I+QI+Q}}(\omega+\omega'')\mathbf{G}^{Tr}_{\mathrm{I+Q+Q'I}}(\omega+\omega'+\omega'')\mathbf{t}_{\mathrm{ID_L}}$$
$$\times \bar{\mathbf{g}}^r_{\mathrm{D_L D_L}}(\omega+\omega'+\omega'')\boldsymbol{\Sigma}^<_{\mathrm{D_L L_L D_L}}(\omega+\omega'+\omega'')\bar{\mathbf{g}}^a_{\mathrm{D_L D_L}}(\omega+\omega'+\omega'')$$
$$\times \mathbf{t}_{\mathrm{D_L I}}\mathbf{G}^{Ta}_{\mathrm{II+Q+Q'}}(\omega+\omega'+\omega'')\mathbf{g}^<_{\mathrm{I+Q'I+Q'}}(\omega+\omega')\mathbf{G}^{Ta}_{\mathrm{II}}(\omega)\mathbf{t}_{\mathrm{ID_R}}\big\} - \text{“}<\leftrightarrow>\text{”}\Big]. \tag{C11}$$

The subscript Q in the index of the reservoir Green's functions indicates that the photon momentum q has to be added to the index and that the index is summed over. While the first trace in the polarization diagram expressions (C7), (C8), and (C9) corresponds to the closed fermion loop, the second trace in the same expressions corresponds to the lower line of the respective diagrams.

APPENDIX D: TUNNELING GREEN'S FUNCTIONS OF SOURCE CHANNEL

In this Appendix, the source channel tunneling Green's functions are presented, which are required to determine the diagrams that contribute due to interchannel interaction (50). These Green's functions develop according to

$$\mathbf{G}^T_{\mathrm{L_L L_L}} = \mathbf{g}_{\mathrm{L_L L_L}} + \mathbf{g}_{\mathrm{L_L L_L}}\boldsymbol{\Sigma}_{\mathrm{L_L D_L L_L}}\mathbf{g}_{\mathrm{L_L L_L}}, \tag{D1}$$

where

$$\boldsymbol{\Sigma}_{\mathrm{L_L D_L L_L}} = \mathbf{t}_{\mathrm{L_L D_L}}\mathbf{G}^T_{\mathrm{D_L D_L}}\mathbf{t}_{\mathrm{D_L L_L}}, \tag{D2}$$

in which

$$\mathbf{G}^T_{\mathrm{D_L D_L}} = \bar{\mathbf{g}}_{\mathrm{D_L D_L}} + \bar{\mathbf{g}}_{\mathrm{D_L D_L}}\mathbf{t}_{\mathrm{D_L I}}\mathbf{G}^T_{\mathrm{II}}\mathbf{t}_{\mathrm{ID_L}}\bar{\mathbf{g}}_{\mathrm{D_L D_L}}. \tag{D3}$$

Upon insertion of (D2) into (D1), application of the Langreth rules, and subsequent collection of all terms, the lesser/greater component of (D1) on the Keldysh contour becomes

$$\begin{aligned}\mathbf{G}^{T<\!/\!>}_{\mathrm{L_L L_L}} &= \big(\mathbf{I}+\mathbf{g}^r_{\mathrm{L_L L_L}}\boldsymbol{\Sigma}^r_{\mathrm{L_L D_L L_L}}\big)\mathbf{g}^{<\!/\!>}_{\mathrm{L_L L_L}}\big(\mathbf{I}+\boldsymbol{\Sigma}^a_{\mathrm{L_L D_L L_L}}\mathbf{g}^a_{\mathrm{L_L L_L}}\big)\\ &+\mathbf{g}^r_{\mathrm{L_L L_L}}\overline{\boldsymbol{\Sigma}}^r_{\mathrm{L_L D_L I}}\big(\mathbf{I}+\mathbf{G}^{Tr}_{\mathrm{II}}\boldsymbol{\Sigma}^r_{\mathrm{ITI}}\big)\mathbf{g}^{<\!/\!>}_{\mathrm{II}}\big(\mathbf{I}+\boldsymbol{\Sigma}^a_{\mathrm{ITI}}\mathbf{G}^{Ta}_{\mathrm{II}}\big)\overline{\boldsymbol{\Sigma}}^a_{\mathrm{ID_L L_L}}\mathbf{g}^a_{\mathrm{L_L L_L}}\\ &+\mathbf{g}^r_{\mathrm{L_L L_L}}\overline{\boldsymbol{\Sigma}}^r_{\mathrm{L_L D_L I}}\mathbf{G}^{Tr}_{\mathrm{II}}\boldsymbol{\Sigma}^{<\!/\!>}_{\mathrm{ID_R I}}\mathbf{G}^{Ta}_{\mathrm{II}}\overline{\boldsymbol{\Sigma}}^a_{\mathrm{ID_L L_L}}\mathbf{g}^a_{\mathrm{L_L L_L}},\end{aligned} \tag{D4}$$

where we defined the tunneling self-energy

$$\overline{\boldsymbol{\Sigma}}_{\mathrm{L_L D_L I}} = \mathbf{t}_{\mathrm{L_L D_L}}\bar{\mathbf{g}}_{\mathrm{D_L D_L}}\mathbf{t}_{\mathrm{D_L I}}. \tag{D5}$$

Inspection of (D4) shows that this Green's function again accounts for equilibration in all components of the system [cf. (36)]. The first line in (D4) contains the bare lesser/greater Green's function of the source lead, and thus accounts for direct equilibration in this lead. The second line describes equilibration after tunneling into the intermediate reservoir region. The third line describes tunneling from the source lead to equilibration in the drain lead, passing both quantum dots. Taking into account only one passage through each quantum dot as in Sec. VI, we neglect the third term of (D4). For the first term of (D4) we employ

$$\big(\mathbf{I}+\mathbf{g}^r_{\mathrm{L_L L_L}}\boldsymbol{\Sigma}^r_{\mathrm{L_L D_L L_L}}\big)\mathbf{g}^{<\!/\!>}_{\mathrm{L_L L_L}}\big(\mathbf{I}+\boldsymbol{\Sigma}^a_{\mathrm{L_L D_L L_L}}\mathbf{g}^a_{\mathrm{L_L L_L}}\big) \to \mathbf{g}^{<\!/\!>}_{\mathrm{L_L L_L}} \tag{D6}$$

[compare (C6)].

APPENDIX E: ENERGY INTEGRALS FOR FINITE-RANGE MODEL INTERACTION

This Appendix contains explicit expressions of integrals of (44) for the finite-range model interaction (35), required to evaluate all diagrams in which a charge carrier that has been excited from the Fermi sea passes through the detector. Upon insertion of (35) into (44), we find

$$\Xi(\omega'') = \nu_0\left[\frac{\Delta x}{\lambda^2\omega''^2+v^2} + \frac{2i\lambda^2 v\omega''}{(\lambda^2\omega''^2+v^2)^2} - \frac{\lambda}{2}\frac{\exp\left[i\frac{\Delta x}{v}\left(i\frac{v}{\lambda}-\omega''\right)\right]}{(iv-\lambda\omega'')^2}\right], \tag{E1}$$

in which we neglect the third term on the right in case $\Delta x \gg \lambda$. Using this approximation, we have

$$\Lambda(\omega'') = \int d\omega''\,\Xi(\omega'') = \nu_0\left[\frac{\Delta x\,\arctan\left(\frac{\lambda\omega''}{v}\right)}{\lambda v} - \frac{iv}{\lambda^2\omega''^2+v^2}\right], \tag{E2}$$

$$\Phi(\omega'') = \int d\omega''\,|\Xi(\omega'')|^2 = \frac{1}{12}\nu_0^2\left[\frac{3(\lambda^2+2\Delta x^2)\arctan\left(\frac{\lambda\omega''}{v}\right)}{\lambda v^3} + \frac{2\lambda^2\omega''}{(\lambda^2\omega''^2+v^2)^2} - \frac{8\lambda^2 v^2\omega''}{(\lambda^2\omega''^2+v^2)^3} + \frac{3\omega''(\lambda^2+2\Delta x^2)}{v^4+\lambda^2 v^2\omega''^2}\right], \tag{E3}$$

as well as

$$\Psi(\omega'') = \int d\omega'' \,\mathrm{Re}[\Xi^*(\omega'')\Xi(\omega_L - \omega_R - \omega'')]$$
$$= \frac{\nu_0^2}{[\lambda^2(\omega_L-\omega_R)^2+4v^2]^3}\Bigg\{\arctan\left(\frac{\lambda\omega''}{v}\right)[\Delta x^2\lambda^4(\omega_L-\omega_R)^4+8v^4(2\Delta x^2-\lambda^2)+2\lambda^2v^2(4\Delta x^2+3\lambda^2)(\omega_L-\omega_R)^2]/\lambda v$$
$$+\arctan\left(\frac{\lambda(\omega''-\omega_L+\omega_R)}{v}\right)[\Delta x^2\lambda^4(\omega_L-\omega_R)^4+8v^4(2\Delta x^2-\lambda^2)+2\lambda^2v^2(4\Delta x^2+3\lambda^2)(\omega_L-\omega_R)^2]/\lambda v$$
$$+\{2v^2(\omega_L-\omega_R)(-2\omega''+\omega_L-\omega_R)[\lambda^2(\omega_L-\omega_R)^2+4v^2][-\lambda^4(\omega_L-\omega_R)^2[-3\omega''^2+3\omega''(\omega_L-\omega_R)+(\omega_L-\omega_R)^2]$$
$$+4v^4+\lambda^2v^2(4\omega''^2+4\omega''(\omega_R-\omega_L)+3(\omega_L-\omega_R)^2)]/(\lambda^2\omega''^2+v^2)[\lambda^2(\omega''-\omega_L+\omega_R)^2+v^2]$$
$$+[\Delta x^2\lambda^4(\omega_L-\omega_R)^6+32v^6+8v^4(2\Delta x^2+3\lambda^2)(\omega_L-\omega_R)^2+4\lambda^2v^2(2\Delta x^2+3\lambda^2)(\omega_L-\omega_R)^4][\log(\lambda^2\omega''^2+v^2)$$
$$-\log[\lambda^2(\omega''-\omega_L+\omega_R)^2+v^2]]/\lambda^2\}/(\omega_L-\omega_R)^3\}. \quad \text{(E4)}$$

[1] N. Ofek, A. Bid, M. Heiblum, A. Stern, V. Umansky, and D. Mahalu, Proc. Natl. Acad. Sci. USA **107**, 5276 (2010).
[2] Y. Ji, Y. Chung, D. Sprinzak, M. Heiblum, D. Mahalu, and H. Shtrikman, Nature (London) **422**, 415 (2003).
[3] P. Roulleau, F. Portier, D. C. Glattli, P. Roche, A. Cavanna, G. Faini, U. Gennser, and D. Mailly, Phys. Rev. B **76**, 161309(R) (2007).
[4] C. de C. Chamon, D. E. Freed, S. A. Kivelson, S. L. Sondhi, and X. G. Wen, Phys. Rev. B **55**, 2331 (1997).
[5] C. Han, J. Park, Y. Gefen, and H.-S. Sim, Nat. Commun. **7**, 11131 (2016).
[6] C. Nayak, S. H. Simon, A. Stern, M. Freedman, and S. Das Sarma, Rev. Mod. Phys. **80**, 1083 (2008).
[7] I. Neder, N. Ofek, Y. Chung, M. Heiblum, D. Mahalu, and V. Umansky, Nature (London) **448**, 333 (2007).
[8] V. Freulon, A. Marguerite, J.-M. Berroir, B. Plaçais, A. Cavanna, Y. Jin, and G. Fève, Nat. Commun. **6**, 6854 (2015).
[9] E. Bocquillon, V. Freulon, F. D. Parmentier, J.-M. Berroir, B. Plaçais, C. Wahl, J. Rech, T. Jonckheere, T. Martin, C. Grenier, D. Ferraro, P. Degiovanni, and G. Fève, Ann. Phys. **526**, 1 (2013).
[10] H. le Sueur, C. Altimiras, U. Gennser, A. Cavanna, D. Mailly, and F. Pierre, Phys. Rev. Lett. **105**, 056803 (2010).
[11] P. Degiovanni, C. Grenier, G. Feve, C. Altimiras, H. le Sueur, and F. Pierre, Phys. Rev. B **81**, 121302(R) (2010).
[12] A. M. Lunde, S. E. Nigg, and M. Büttiker, Phys. Rev. B **81**, 041311(R) (2010).
[13] D. L. Kovrizhin and J. T. Chalker, Phys. Rev. B **84**, 085105 (2011).
[14] E. Bocquillon, V. Freulon, J.-.M. Berroir, P. Degiovanni, B. Plaçais, A. Cavanna, Y. Jin, and G. Fève, Nat. Commun. **4**, 1839 (2013).
[15] T. Krähenmann, Electron Transfer Between Quantum Dots, Doctoral Dissertation, ETH Zürich, 2017.
[16] T. Krähenmann, S. G. Fischer, M. Röösli, T. Ihn, C. Reichl, W. Wegscheider, K. Ensslin, Y. Gefen, and Y. Meir, Nat. Commun. **10**, 3915 (2019).
[17] R. H. Rodriguez, F. Parmentier, P. Roulleau, U. Gennser, A. Cavanna, F. Portier, D. Mailly, and P. Roche, arXiv:1903.05919.
[18] D. Ferraro, B. Roussel, C. Cabart, E. Thibierge, G. Fève, C. Grenier, and P. Degiovanni, Phys. Rev. Lett. **113**, 166403 (2014).
[19] D. L. Kovrizhin and J. T. Chalker, Phys. Rev. Lett. **109**, 106403 (2012).
[20] S. Takei, M. Milletarì, and B. Rosenow, Phys. Rev. B **82**, 041306(R) (2010).
[21] M. Acciai, A. Calzona, G. Dolcetto, T. L. Schmidt, and M. Sassetti, Phys. Rev. B **96**, 075144 (2017).
[22] J. T. Chalker, Y. Gefen, and M. Y. Veillette, Phys. Rev. B **76**, 085320 (2007).
[23] I. P. Levkivskyi and E. V. Sukhorukov, Phys. Rev. B **85**, 075309 (2012).
[24] Y. Meir and N. S. Wingreen, Phys. Rev. Lett. **68**, 2512 (1992).
[25] C. Neuenhahn and F. Marquardt, New J. Phys. **10**, 115018 (2008).
[26] J. Maciejko, *An Introduction to Nonequilibrium Many-Body Theory* (Springer, Berlin, 2007).
[27] H. Haug and A. Jauho, *Quantum Kinetics in Transport and Optics of Semiconductors*, Springer Series in Solid-State Sciences (Springer, Berlin, 2007).
[28] R. Guyon, P. Devillard, T. Martin, and I. Safi, Phys. Rev. B **65**, 153304 (2002).
[29] O. Zilberberg, A. Carmi, and A. Romito, Phys. Rev. B **90**, 205413 (2014).
[30] D. Bischoff, M. Eich, O. Zilberberg, C. Rössler, T. Ihn, and K. Ensslin, Nano Lett. **15**, 6003 (2015).
[31] C. Altimiras, H. le Sueur, U. Gennser, A. Cavanna, D. Mailly, and F. Pierre, Phys. Rev. Lett. **105**, 226804 (2010).
[32] H. Duprez, E. Sivre, A. Anthore, A. Aassime, A. Cavanna, A. Ouerghi, U. Gennser, and F. Pierre, Phys. Rev. X **9**, 021030 (2019).
[33] I. P. Levkivskyi and E. V. Sukhorukov, Phys. Rev. Lett. **103**, 036801 (2009).
[34] D. B. Gutman, Y. Gefen, and A. D. Mirlin, Phys. Rev. B **81**, 085436 (2010).
[35] D. B. Gutman, Y. Gefen, and A. D. Mirlin, Phys. Rev. Lett. **105**, 256802 (2010).
[36] D. B. Gutman, Y. Gefen, and A. D. Mirlin, J. Phys. A: Math. Theor. **44**, 165003 (2011).
[37] I. V. Protopopov, D. B. Gutman, and A. D. Mirlin, Lith. J. Phys. **52**, 165 (2012).
[38] I. V. Protopopov, D. B. Gutman, and A. D. Mirlin, Phys. Rev. Lett. **110**, 216404 (2013).
[39] G. Mahan, *Many-Particle Physics*, Physics of Solids and Liquids (Springer, Berlin, 2000).